REPORT DOCUMENTATION PAGE

Form Approved
OMB No. 0704-0188

1. REPORT DATE *(DD-MM-YYYY)*	**2. REPORT TYPE**	**3. DATES COVERED** *(From - To)*
30 November 2015	Master's Thesis	01 Nov 2015 – 30 Nov 2015

4. TITLE AND SUBTITLE
Advances in Turbulent Combustion Dynamics Simulations in Bluff-Body Stabilized Flames-Body Stabilized Flames

5a. CONTRACT NUMBER

5b. GRANT NUMBER

5c. PROGRAM ELEMENT NUMBER

6. AUTHOR(S)
Jonathan Tovar

5d. PROJECT NUMBER

5e. TASK NUMBER

5f. WORK UNIT NUMBER
Q1FZ

7. PERFORMING ORGANIZATION NAME(S) AND ADDRESS(ES) AND ADDRESS(ES)

Air Force Research Laboratory (AFMC)
AFRL/RQR
5 Pollux Drive
Edwards AFB, CA 93524-7048

8. PERFORMING ORGANIZATION REPORT NO.

9. SPONSORING / MONITORING AGENCY NAME(S) AND ADDRESS(ES)

Air Force Research Laboratory (AFMC)
AFRL/RQR
5 Pollux Drive
Edwards AFB, CA 93524-7048

10. SPONSOR/MONITOR'S ACRONYM(S)

11. SPONSOR/MONITOR'S REPORT NUMBER(S)
AFRL-RQ-ED-OT-2015-414

12. DISTRIBUTION / AVAILABILITY STATEMENT
Approved for public Release; distribution unlimited. (November 2015)

13. SUPPLEMENTARY NOTES
This is Master's thesis work by Jonathan Tovar in fulfilment of graduate school requirements at the University of California Los Angeles. PA Clearance #15682 Clearance Date 11/24/2015

14. ABSTRACT

This work examines the three main aspects of bluff-body stabilized flames: stationary combustion, lean blow-out, and thermo-acoustic instabilities. For the cases of stationary combustion and lean blow-out, an improved version of the Linear Eddy Model approach is used, while in the case of thermo-acoustic instabilities, the effect of boundary conditions on the predictions are studied. The improved version couples the Linear Eddy Model with the full-set of resolved scale Large Eddy Simulation equations for continuity, momentum, energy, and species transport. In traditional implementations the species equations are generally solved using a Lagrangian method which has some significant limitations. The novelty in this work is that the Eulerian species concentration equations are solved at the resolved scale and the Linear Eddy Model is strictly used to close the species production term. In this work, the improved Linear Eddy Model approach is applied to predict the flame properties inside the Volvo rig and it is shown to over-predict the flame temperature and normalized velocity when compared to experimental data using a premixed single step global propane reaction with an equivalence ratio of 0.65. The model is also applied to predict lean blow-out and is shown to predict a stable flame at an equivalence ratio of 0.5 when experiments achieve flame extinction at an equivalence ratio of 0.55. The improved Linear Eddy Model is, however, shown to be closer to experimental data than a comparable reactive flow simulation that uses laminar closure of the species source terms. The thermo-acoustic analysis is performed on a combustor rig designed at the Air Force Research Laboratory. The analysis is performed using a premixed single step global methane reaction for laminar reactive flow and shows that imposing a non-physical boundary condition at the rig exhaust will result in the suppression of acoustic content inside the domain and can alter the temperature contours in non-physical ways. It can be concluded from this work that it is important to include the proper exhaust configuration for reacting thermo-acoustic calculations so that non-physical boundary conditions do not compromise the solution.

15. SUBJECT TERMS
N/A

16. SECURITY CLASSIFICATION OF:			**17. LIMITATION OF ABSTRACT**	**18. NUMBER OF PAGES**	**19a. NAME OF RESPONSIBLE PERSON**
					V. Sankaran
a. REPORT	**b. ABSTRACT**	**c. THIS PAGE**	SAR	90	**19b. TELEPHONE NO** *(include area code)*
Unclassified	**Unclassified**	**Unclassified**			N/A

Standard Form 298 (Rev. 8-98)
Prescribed by ANSI Std. 239.18

University of California
Los Angeles

Advances in Turbulent Combustion Dynamics Simulations in Bluff-Body Stabilized Flames

A thesis submitted in partial satisfaction
of the requirements for the degree
Master of Science in Aerospace Engineering

by

Jonathan Tovar

2015

Abstract of the Thesis

Advances in Turbulent Combustion Dynamics Simulations in Bluff-Body Stabilized Flames

by

Jonathan Tovar

Master of Science in Aerospace Engineering

University of California, Los Angeles, 2015

Professor Ann R. Karagozian, Chair

This work examines the three main aspects of bluff-body stabilized flames: stationary combustion, lean blow-out, and thermo-acoustic instabilities. For the cases of stationary combustion and lean blow-out, an improved version of the Linear Eddy Model approach is used, while in the case of thermo-acoustic instabilities, the effect of boundary conditions on the predictions are studied. The improved version couples the Linear Eddy Model with the full-set of resolved scale Large Eddy Simulation equations for continuity, momentum, energy, and species transport. In traditional implementations the species equations are generally solved using a Lagrangian method which has some significant limitations. The novelty in this work is that the Eulerian species concentration equations are solved at the resolved scale and the Linear Eddy Model is strictly used to close the species production term.

In this work, the improved Linear Eddy Model approach is applied to predict the flame properties inside the Volvo rig and it is shown to over-predict the flame temperature and normalized velocity when compared to experimental data using a premixed single step global propane reaction with an equivalence ratio of 0.65. The model is also applied to predict lean blow-out and is shown to predict a stable flame at an equivalence ratio of 0.5 when experiments achieve flame extinction at an equivalence ratio of 0.55. The improved Linear Eddy Model is, however, shown to be closer to experimental data than a comparable reactive flow simulation that uses laminar closure of the species source terms.

The thermo-acoustic analysis is performed on a combustor rig designed at the Air Force Research Laboratory. The analysis is performed using a premixed single step global methane reaction for laminar reactive flow and shows that imposing a non-physical boundary condition at the rig exhaust will result in the suppression of acoustic content inside the domain and can alter the temperature contours in non-physical ways. It can be concluded from this work that it is important to include the proper exhaust configuration for reacting thermo-acoustic calculations so that non-physical boundary conditions do not compromise the solution.

The thesis of Jonathan Tovar is approved.

Jeff Eldredge

Xiaolin Zhong

Venkateswaran Sankaran

Ann R. Karagozian, Committee Chair

University of California, Los Angeles

2015

This work is dedicated to my girlfriend, Michelle Sirisuk. How she managed to survive my completing this work will forever remain a mystery.

Table of Contents

List of Figures

List of Tables

Acknowledgments

This research has been supported by the Air Force Research Laboratory (AFRL/RQ) under subcontract RS131108 from ERC, Inc., with Dr. Venkateswaran Sankaran as the technical lead.

I would like to acknowledge all of the people instrumental in the preparation of this thesis. Especially to my committee members: Dr. Jeff Eldredge, Dr. Xiaolin Zhong, Dr. Venkateswaran Sankaran, and Dr. Ann Karagozian. I would specifically like to express my deepest thanks to Ann Karagozian for taking a chance on me and always believing that I can accomplish whatever I set my mind to.

I would also like to thank all of my co-workers at the AFRL. They were always there to provide assistance in any way possible. If it were not for them I know that I could not have completed this thesis. These lab members include: Kevin Brown, future Dr. Ayaboe Edoh, Dr. Farhad Davoudzadeh, and Dr. Ananda Himansu. I would specifically like to thank Dr. Matthew Harvazinski and Dr. Nathan Mundis for acting as additional advisers throughout this process. Their assistance played a vital role in me completing this work.

I would also like to thank all of my friends at Absolute Technologies Incorporated for encouraging me to go back to graduate school and complete this degree. These people include: Bradley Bear Downing, Kaitlyn Zekanovic, Tom Davis, Dwight Howard, Sammy Prum, Nara Prum, Tim Berquist, Bill Beverage, Brittany Beverage, Alison Tovar and pretty much everyone who works there. I want to specifically extend my deepest gratitude to Vedran Zekanovic for always being there to encourage me through the tough times. His words of wisdom gave me the strength to handle the difficult situations that arose during this journey.

To my family and friends for always supporting me throughout this work: my parents Anna and David Sr. Tovar, my brothers David Jr., Samuel, and Thomas. My friends include but are not limited to: Lucas Hendershot, Nicholas Briones, Andrew Florin, Daniel Zorub, Berton Vite, Stephan Coffer, Yuan Yi, Cool Chill Cheng, Nipun Kuzhikattil, and Yi Yan. Finally, I would be remiss if I did not mention my amazing girlfriend Michelle Sirisuk for her love and support throughout this process. Thank you all so very much.

Nomenclature

$\bar{\Delta}$	LES filter width
Δs	LEM node spacing
$\dot{\omega}$	Species production term
ℓ	Eddy length
η	Kolmogorov length scale
λ	Thermal conductivity coefficient
ω	Specific rate of dissipation
ϕ	Equivalence ratio
ρ	Density
$\tilde{u}$	LES resolved velocity
C_p	Specific heat at constant pressure
D	Diffusion coefficient
f	Stirring frequency
h_0	Total enthalpy
$h^0_{f,k}$	Heat of formation
$h_{s,k}$	Sensible enthalpy
k	Sub-grid kinetic energy
N_{LEM}	Number of LEM cells
P	Pressure
T	Temperature
u''	LES sub-grid velocity
W_{mix}	Molecular weight of mixture
Y	Species mass fraction

CHAPTER 1

Introduction

In air-breathing propulsion systems it is vital to maintain a sustained combustion process in fuel-air flows that travel at speeds exceeding the normal burning velocity [1]. A device that has been shown to stabilize and maintain a flame in these flows is a bluff-body. A bluff-body is an object immersed in a fluid flow that causes the flow to travel around it, creating highly separated flow downstream of the object which can form a closed recirculation region. Bluff-bodies have been commonly used in premixed combustion applications because the recirculation region behind the object serves to capture heat from the reactive process that continually ignites the incoming mixture of fuel and oxidizer therefore stabilizing the flame. It is important to understand the flow fields because turbulent bluff-body stabilized flames are used in many aerospace propulsion systems including gas turbine engines, afterburners, ramjets, and scramjets.

For over a decade, airbreathing engine development has emphasized improving efficiency and reducing emissions as the driving factors behind new designs. Recent engines have been designed to run leaner in an effort to lessen the environmental impact of emissions such as nitrogen oxides (NOx). A lean engine operates with an O/F ratio less than the stoichiometric ratio, and produces lower temperature flames that reduce thermal nitric oxide (NO). Lean combustion also emits fewer unburned hydrocarbons (UHCs) because the excess air generally results in complete consumption of the fuel [2]. Unfortunately, combustion in this lean regime is difficult to maintain due to the flames being more susceptible to instabilities and lean blow off, especially for bluff body stabilized flames. Since fuel efficient bluff body turbulent combustion is and will continue to be important to many aerospace vehicles, there is a need for accurate prediction of turbulent combusting flows in this regime. This need has led to the

research and development of improved computational fluid dynamics (CFD) methods and turbulent combustion models. Improvements of these methods can not only have significant monetary savings but also serve as an important tool for the design of new efficient engines that operate safely.

This thesis will review several turbulent combustion models and their predictive capability with regards to bluff body stabilized flames. A new model is proposed and integrated into an established CFD code. The combined solver is then applied to a bluff-body stabilized flame problem with comparison to extensive experimental results in order demonstrate its viability for the prediction of flow properties and phenomena such as lean blow-out. Additionally, a study is also conducted on how boundary conditions and experimental geometry affect reacting and non-reacting predictions of the thermo-acoustic interactions inside a two-dimensional duct.

1.1 Turbulent Combustion Modeling

A complete simulation of all relevant spatial and temporal scales is called direct numerical simulation (DNS). In a DNS there is no need for a turbulence or turbulent combustion model [3]. All spatial scales from the integral scale down to the Kolmogorov scale are captured on the computational mesh. Many practical aerospace problems, including propulsion, are associated with high Reynolds numbers and extremely small Kolmogorov length scales. The number of grid points needed is excessive and therefore computationally very expensive. DNS also requires small time steps that adds additional expense. As a result of this required fine resolution, DNS is not practical for most relevant aerospace problems and is therefore limited in its application to academic problems.

Without DNS, some type of model is required to capture the effects of the turbulent fine scales that are not being directly computed. One such modeling approach uses the Reynolds Averaged Navier-Stokes (RANS) equations, which have long been used in CFD simulations to predict turbulent flows. In RANS all turbulence scales are modeled, which makes it an attractive model because relatively coarse grids can be used. The coarse grids and minimal

cost of the RANS simulation make it computationally tractable. For some applications it has been shown to produce reasonable results, especially for steady, non-reacting flows. It has also been shown to be unreliable in flows involving typical propulsion flowfield conditions such as those with adverse pressure gradients, flow separation, recirculation, and unsteady flame dynamics [4]. Underlying reasons for the inaccuracies are a result of the assumptions inherent in deriving the RANS equations. The RANS equations are derived by decomposing the fluid properties (i.e. pressure, density, velocity and species) in the Navier-Stokes equations into mean and a fluctuating component. The resulting equations are time averaged and contain additional terms which require models to close them in order to solve the equations. Many different models such as the $k-\epsilon$ and the $k-\omega$ [5] models have been proposed. Each model has shown success for specific applications but no model is universally applicable, generally because they employ adjustable constants that are configuration specific. Additional modeling is required for reacting flows when the species equations are solved in combination with the momentum and the energy equations. It is clear that the characteristics of the model itself becomes vitally important to the accuracy of the solution. In combustion, the heat is released at the small scales and affects the larger scales so it is important to capture the interaction between these scales. In RANS models there is no distinction between the large and small scales which means that the modeled terms in the RANS equations like the velocity-species and temperature-species interactions cannot accurately capture the interaction between scales [6].

A natural middle-ground between these two modeling approaches is to accurately resolve a portion of the turbulence and model only the smallest scales. The large eddy simulation (LES) framework was developed with this in mind. LES is designed so that it resolves the large scale turbulent structures and models the small scale structures. In order to obtain the scale separation in a reactive flow, the governing equations and species equations are Favre-filtered[7] which then allows the turbulent-kinetic-energy containing eddies to be resolved and the smaller scales to be modeled. LES has an advantage over RANS because it can represent the interaction between the resolved scale and the unresolved (modeled) scale [6]. The filtering operation, for LES, like in Reynolds averaging, introduces terms that are not

closed by the equations and therefore need turbulence and especially turbulence combustion models. The latter refers to the closure of the species source term in order to accommodate the influence of the sub-grid turbulent fluctuations on the combustion.

There are many turbulent combustion models for LES that have been examined in the literature. Flamelet [8, 9], linear eddy modeling (LEM) [10, 11, 12, 13, 14, 15, 16], and the transported-probability density function (PDF) [17, 18, 19, 20] are three of the most widely used models in the literature and have shown success in modeling different phenomena. A brief description of each of these sub-grid models will be discussed to identify the key underlying assumptions of each model.

1.1.1 Steady Laminar Flamelet Model

The steady laminar flamelet model employs the notion that a turbulent flame front can be modeled using a locally one-dimensional strained flamelet structure inside a turbulent flow. Flamelets replace the species and energy conservation equations with a single conserved scalar equation, typically in terms of mixture fraction. Key to this model is the assumption that the chemical kinetics time-scales are smaller than the smallest turbulent time scales [8]. One major advantage of flamelets is that the conserved scalar equation replaces a large number of species transport equations and is therefore less computationally expensive to solve compared with other models. Instead, the flamelet approach relies on a pre-computed flamelet library[9] in order to determine local species mass fractions, thermodynamic and transport properties, temperature, and source terms.

The flamelet model involves numerous assumptions which limit its applicability. Two key assumptions are required in order to reduce the species and energy equations to the conserved scalar form, which are, a constant pressure and a unity Lewis number, where the Lewis number is the ratio of thermal diffusion to species diffusion. Flamelet models are therefore only valid in a low Mach number regime. This approximation further means that the thermal diffusivity and all species mass diffusivities are equal, thereby removing differential mass diffusion which is important for many reactive flows. Viscous dissipation is

also explicitly removed from the conservation equations in the flamelet modeling. As a result of these assumptions, unsteady reactive phenomena and coupling to acoustic speeds will not be correctly predicted by the model. An accurate representation of acoustic speeds is essential for the prediction of thermo-acoustic instabilities which are an important consideration in the design and evaluation of bluff-body stabilized propulsion systems.

The flamelet procedure starts with a pre-processing step where the flamelet equations are solved and tabulated in terms of mixture fraction and local scalar dissipation rate[8]. Solving these equations and tabulating the data allow for rapid access to the value for species mass fraction, temperature, and thermodynamic and transport properties. The flamelet solutions are based on a canonical configuration like a counterflow diffusion flame or a premixed flame[8]. Next, the source term-free, conserved scalar equation is solved using the local flow conditions to obtain a value for the conserved scalar, which is a parameter constructed from combinations of species mass fractions and temperature. Using the calculated conserved scalar value and the scalar dissipation rate which is proportional to the local rate of strain, the relevant scalars are obtained from the tabulated data. After a given scalar is determined, it then needs to be filtered to obtain the mass fraction variables. In order to perform this step, a β joint probability density function (PDF) function for the conserved scalar is typically used [8]. The reactive scalar and conserved scalar are then integrated to obtained a filtered reactive scalar quantity.

The β PDF is a further limitation of the flamelet method because it is a simplification compared to the distribution functions of other turbulent combustion closure methods such as LEM and transported PDF. Additionally, there is some confusion about flamelets in regions of flow that have both premixed and non-premixed combustion because the correct canonical configuration to use in each domain is unclear. Finally, the tabulated data are computed based upon the inlet conditions of the reactants and may not be truly representative of the local flow conditions.

1.1.2 Transported Probability Density Function Model

The transported probability density function method models the non-linear effects in turbulent combusting flows using a one-point, one-time joint PDF for a given set of flow variables [17, 18, 19, 20]. The PDF method was originally developed to be used as a RANS closure and more recently is being applied to LES [21]. Currently, the most advanced PDF methods incorporate the velocity, the turbulence frequency, and the composition as the flow variables. A main advantage of this method is the chemical source term is represented exactly in the species equations, unlike in other turbulent combustion models, where the source terms need to be closed by introducing other model assumptions. These source terms are not dependent on spatial or temporal correlations and, therefore, they are ideal to be represented by a single-point, one-time PDF approach.

The PDF equation is a transport equation that is applicable to premixed and partially premixed flames. The acceleration, the velocity and the composition (chemical source term) in the equation are solved using local fluid values. The viscous effects, the fluctuating pressure gradients, and the molecular diffusion require models to close the PDF equation. The current area of research in PDF based methods is to develop improved models to capture the mixing and diffusion [22, 23]. The transported PDF method is modeled using a low Mach number or constant pressure approximation that limits its applicability to many aerospace relevant flows.

The PDF equation is solved using Lagrangian methods due to the large number of independent variables involved in these equations. Particle-based method such as Monte Carlo methods are used because finite element and volume methods are much more computationally expensive [17]. The most significant disadvantage of the PDF method is that the large number of independent variables involved in solving the equations make this method computationally expensive. In addition, obtaining a proper mixing model for reacting flows has been a limitation of this sub-grid model.

1.1.3 Linear Eddy Model (LEM)

The linear eddy modeling approach was developed by Alan Kerstein et al. [10, 11] to predict scalar mixing in turbulent flows by stochastically representing the effect of turbulence on a scalar profile at all relevant physical length scales. LEM was first tested as a turbulence model and produced accurate results; it was later adapted to model turbulent combustion [12, 13]. The LEM approach is a multi-scale model that embeds a one-dimensional grid in the sub-grid of the multi-dimensional CFD mesh. The LEM grid is used to solve the conservation equations for the species and the low Mach number form of the energy equation. The orientation of the LEM line is such that it is parallel to the maximum species gradient within each LES cell. The three physical phenomena described by the LEM equations are turbulent stirring/advection, molecular diffusion, and combustion. An attractive feature of the LEM approach is that the full species equations are solved and not approximated as in other sub-grid models, although the solution is obtained in one-dimension.

A unique feature of LEM is that the turbulent stirring is modeled stochastically using a rearrangement process called a triplet map [10]. The triplet map simulates the effect that the inertial range turbulence has on a scalar profile [15]. The map shrinks the one-dimensional scalar profile into a third of the original length and then fills the interval with two additional compressed copies of the profile. The mapping process mimics the effect of a vortex crossing while maintaining complete species conservation. The frequency and the location of the stirring event are chosen stochastically using probability distribution functions [11]. The molecular diffusion in the LEM is accounted for using using Fick′s law with the Hirschfelder and Curtiss approximation, wherein a correction velocity is added to the molecular diffusion to ensure conservation of mass for all species [7].

LEM is implemented as the sub-grid model for LES to form the LEM-LES method. LEM-LES solves the filtered form of the continuity, momentum and energy equations at the resolved scale and solves LEM at the unresolved scale. It solves separate energy equations at the resolved and unresolved scales. Solving two energy equations can produce an inconsistent temperature between the two scales. In the sub-grid, a low Mach form of the energy equation

implies that the pressure is constant in each LEM cell. The temperature calculated at the sub-grid level is erased after each physical time step, and serves only to integrate the species transport equation along the LEM line.

LEM-LES does not solve the Eulerian form of the species transport equations in the resolved scale. Rather, it uses a process called Lagrangian splicing to account for the species transport between LES cells [14]. Splicing divides the mass flux of each LEM line into individual inflow and outflow contributions so the quantity of mass entering and leaving each LEM line is tracked. The mass transfer is accomplished by using the calculated outflux to remove the corresponding number of LEM cells from the output end of the LEM line. Next, the mass influx is used to add the outflux LEM cells from other LEM lines onto the input side of the LEM line. After the mass has been transferred between LES cells, the number of LEM cells within the LEM domain has changed as a results of the splicing. Finally, the LEM domain is re-gridded in order to maintain a uniform LEM mesh [24].

It is important to stress that in LEM-LES the Eulerian species equations are not solved at the resolved scale but instead the species transport is accounted for solely in LEM model. The Lagrangian splicing process has an adherent randomness due to the arbitrary distribution of mass between LES cells. This random distribution of mass occurs because the one-dimensional LEM line is interacting in a multidimensional space. Additionally, the large scale advection process only accounts for advection of mass and does not incorporate the large scale diffusion that takes place between LES cells which means that the species equations do not converge to the correct DNS solution in the limit of very fine grids.

1.2 Bluff-Body Stabilization of Flames

As noted earlier, flames stabilized by bluff-bodies are used in many aerospace propulsion systems. As a result there have been numerous computational studies to assess the predictive capability of CFD tools to predict key flow physics. The difficulties in these problems arise due to the complex vortex dynamics that are seen during stable and unstable combustion [25, 26]. Additionally the challenge of predicting phenomena such as lean blow-out and

thermoacoustics provides added difficulty to state-of-the-art CFD codes because they are inherently unsteady phenomena that have a strong dependence on local flow conditions and can often not be captured by steady state simulations. The challenges involved in computationally predicting the physical flow parameters arise because the CFD solution is greatly influenced by the numerical scheme and the turbulent combustion closure. Efforts to improve CFD predictions of bluff-body stabilized flames have been tested using a number of canonical configurations such as the Volvo rig [27, 28, 29] which is a rectangular duct that contains an equilateral triangle-shaped bluff-body flame holder.

The effect of the numerical discretization scheme on the predictions of the Volvo rig flowfield was studied by Cocks et al. [30], and the results showed that grid dependency and numerical errors can greatly impair the predictive capabilities of the LES. The results showed that despite using the same grid, turbulence model, and flow parameters, different numerical schemes (all of which are formally second order accurate) can produce remarkably different time-dependent results.

The three main phenomena of interest in bluff-body stabilized flames are stationary combustion, lean blow-out, and thermo-acoustic instabilities. The accurate prediction of flow properties in these regimes is heavily dependent on the turbulent combustion model used in the solver. As a result, there has been much focus in past research on applying a wide range of turbulent combustion models to bluff-body stabilized flames to asses their validity in predicting flow properties in these three regimes.

Turbulent combustion modeling studies have mainly focused on profile comparisons of the root-mean-square values of the fluctuating temperature and the velocity in stable premixed flows. One of the earliest studies to predict flow inside the Volvo configuration using LES was performed by Fureby and Möller [31]. The goal of this study was to investigate the effect that sub-grid models have on the predictive capabilities of LES. Their results indicated that LES is capable of predicting most significant flow features, including unsteady flow structures.

Flamelets are an attractive choice for combustion modeling due to the low computational cost compared to many other models. Fureby [32] applied both the propagation-based

flamelet model and the filtered flamelet model to premixed bluff body stabilized flames. The results showed that both of the flamelet models produced reasonable comparison; however, the filtered flamelet model was more sensitive to the grid resolution. Additional research in flamelets was conducted by Baudoin et al. [33] in which the G-equation model and four finite rate chemistry models were employed. These chemistry models include the partial stirred reactor model (PaSr), thickened flame model (TFM), eddy dissipation concept (EDC), and presumed probability density function (PPDF). These were compared using the Volvo rig geometry. The results showed that all four finite rate models had very good agreement with each other and experimental data in the temperature, the velocity, and the species concentration despite being significantly different modeling approaches. On the other hand, the flamelet G-equation model had a more noticeable deviation with experimental data compared to the finite rate models.

Porumbel and Menon compared the eddy break-up (EBU) and LEM as closure conditions for the LES resolved scale equations [34]. The simulations were run with both reacting and non-reacting flow using the Volvo rig geometry. The reacting simulation used a premixed propane-air mixture at an equivalence ratio, ϕ, of 0.65. Both models predicted Von Kármán vortex shedding and other flow parameters accurately for the non-reacting flow case. For the reacting flow case, both models predicted the time-averaged velocity with good accuracy, while the EBU sub-grid model failed to predict the turbulent fluctuations in the flow field. Additionally, the EBU under-predicts the centerline temperature due to insufficient prediction of turbulent mixing rate.

Further work was done by Jones et al. [35] using a sub-grid joint PDF in conjunction with the Eulerian stochastic field method as the turbulent combustion closure. The results showed good agreement with the experimental results and showed that LES accurately predicts premixed combustion fluid properties when coupled with an appropriate sub-grid model. From analyzing past work it is possible to conclude that accurately predicting the mean flow parameters (temperature, velocity, species concentration) in a stable premixed turbulent combustion problem is possible with a wide number of closures.

Research into lean blowout prediction in premixed bluff body stabilized flames was per-

formed by Gokulakrishnan et al. [36] on the experimental setup by Kiel et al. [37] at the Air Force Research Laboratory (AFRL). This experiment differs from the Volvo experiment in that the bluff body is a V-gutter instead of an equilateral triangle. CFD calculations were performed using the laminar chemistry model (LCM) [38] and EDC [39] models to determine the equivalence ratio that computationally predicts lean blowout. The results showed that LES coupled with EDC showed blow-out at an equivalence ratio of 0.6, which matches the observed experimental results. The laminar chemistry model did not blowout until a much lower equivalence ratio of 0.45. This research demonstrates that the turbulence-chemistry interactions play a key role in predicting the wake region behind the flame holder, and therefore flame stability.

The effect of boundary conditions and domain configuration was researched by Ma et al. [40] on the Volvo rig to analyze the prediction of thermo-acoustic phenomena. Two simulations were run, one with a full Volvo rig domain and a constant pressure outlet boundary condition, the other simulation used a partial domain with an impedance boundary condition for the outlet. The simulations were performed using the FLUENT commercial software package with the flamelet model being used for turbulent combustion closure. The focus of the work was to compare the pressure wave amplitude and frequency content for the two different outlet boundary conditions. The results showed that both cases had good agreement in terms of the predicted frequency but the magnitude of the oscillations was different for some equivalence ratios. The results also showed an increase in pressure oscillations with an increase in equivalence ratio.

1.3 Computational Fluid Dynamics Solver

The CFD code used in the present research is the General Equation and Mesh Solver, or simply GEMS. GEMS is a CFD code that was designed by Charles Merkle's group at Purdue University and is actively being used by Purdue and the Air Force Research Laboratory to perform both reacting and non-reacting CFD calculations in rocket and turbine engines [41, 42]. The code uses a finite volume method to solve the continuity, the Navier-Stokes,

and the energy equations with second order accuracy in both time and space. In addition, GEMS is able to handle turbulence and combustion by solving the species conservation equation and turbulence model equations. For the turbulence model equations GEMS uses the $k-\omega$ model which describes the turbulent kinetic energy and turbulent dissipation in the flow, respectively. The combustion is modeling using a laminar flame rate model that is a function of the mean temperature, the pressure, and the species concentration [42].

GEMS uses a combination of RANS and LES called Detached Eddy Simulation (DES) [42] to capture turbulent flow fields. DES uses RANS in the near-wall boundary layer region, where the RANS model performs efficiently in cells with high aspect ratios. On the other hand, LES is implemented in areas away from the boundary layer where the grid resolution supports the turbulent scales [42], thereby capturing the unsteady flame dynamics in regions where combustion is dominant.

1.4 Thesis Objectives

The goal of this thesis is to analyze the three main aspects of bluff-body stabilized flames; stationary combustion, lean blow-out, and thermo-acoustic instabilities. In the cases of stationary combustion and lean blow-out, an improved version of the LEM model is used, while in the case of thermo-acoustic instabilities, the effects of boundary conditions on the predictions are studied. LEM was chosen because it has validity for all flame regimes and is a multi-scale approach that solves the full set of species equations at the sub-grid level, albeit in one-dimension.

This thesis considers an improved formulation of the LEM by coupling it with a full-set of resolved scale LES equations for continuity, momentum, energy, and species transport. The main difference from past implementations is that the species concentration equations are solved at the resolved scale, which includes diffusion and advection. In the past, the species concentration calculations have been completely confined to the sub-grid LEM model and the transport of species between LES cells only accounted for advection. This implementation uses LEM to obtain a closure value for the average species production term in the filtered

species equations at the resolved scale.

In addition to improving LEM, this thesis analyzes the effect of boundary conditions and facility geometry for studying thermo-acoustics in bluff body stabilized flames. Many CFD studies have been performed previously using the Volvo rig geometry but they have typically not modeled the farfield downstream of the duct exit. Instead, a boundary condition has been set at the duct exit. The present study seeks to determine if physical and computational boundary conditions affect the solution inside the duct by modeling the exhaust region for both reacting and non-reacting fluid flows.

The chapters for the thesis are organized as follows:

- Chapter 2 provides a detailed description of the LEM approach. First, the general equations are derived. Next, the numerical implementation is discussed. Finally, the assumptions used in LEM are explicitly stated so the applicability of LEM can be established.

- Chapter 3 tests the predictions of the LEM model for a single sub-grid cell. This section focuses on verifying that the model has been properly implemented and that diffusion, stirring, and combustion processes function correctly.

- Chapter 4 uses the integrated LEM-LES solver to simulate flow in the Volvo rig. The results for temperature, velocity, and lean blow-out equivalence ratio are compared with experimental data.

- Chapter 5 analyzes the effect of boundary conditions and facility geometry on bluff body stabilized flames using the geometry of an experimental rig at AFRL.

- Chapter 6 concludes the research by assessing the advantages and disadvantages of the improved LEM. Lastly, a proposal for future LEM improvements is made.

CHAPTER 2

LEM Approach

The filtered species production term in the LES species transport equation is difficult to calculate in turbulent combustion because it is no longer a function of $\tilde{P}$, $\tilde{T}$, and $\tilde{Y}$ as in laminar combustion and therefore requires a model for closure. The linear eddy model is a multi-scale model used to obtain the filtered species production term. The implementation of the LEM presented in this work differs in some key ways from other implementations in the literature and is therefore described in detail in this chapter.

2.1 LES Equations

Large eddy simulations (LES) solve the filtered conservation equations. The Favre-filtered form of the conservation laws for mass, momentum, energy, and species transport equations are [7]:

$$\frac{\partial \bar{\rho}}{\partial t} + \frac{\partial}{\partial x_i}\left(\bar{\rho}\widetilde{u}_i\right) = 0 \tag{2.1}$$

$$\frac{\partial}{\partial t}\left(\bar{\rho}\widetilde{u}_i\right) + \frac{\partial}{\partial x_j}\left(\bar{\rho}\widetilde{u}_j\widetilde{u}_i\right) = -\frac{\partial \bar{p}}{\partial x_i} + \frac{\partial}{\partial x_j}\left[\bar{\tau}_{ji} - \bar{\rho}\left(\widetilde{u_j u_i} - \widetilde{u}_j\widetilde{u}_i\right)\right] \tag{2.2}$$

$$\frac{\partial}{\partial t}\left(\bar{\rho}\widetilde{h}_0\right) + \frac{\partial}{\partial x_j}\left(\bar{\rho}\widetilde{u}_j\widetilde{h}_0\right) = \frac{\partial \bar{p}}{\partial t} + \frac{\partial}{\partial x_j}\left(\widetilde{u}_i\bar{\tau}_{ij} - \bar{q}_i + \left(\widetilde{u_i\tau_{ij}} - \widetilde{u}_i\bar{\tau}_{ij}\right) - \bar{\rho}\left(\widetilde{u_j h_0} - \widetilde{u}_j\widetilde{h}_0\right)\right) \tag{2.3}$$

$$\frac{\partial}{\partial t}\left(\bar{\rho}\widetilde{Y}_k\right) + \frac{\partial}{\partial x_j}\left(\bar{\rho}\widetilde{u}_j\widetilde{Y}_k\right) = \overline{\dot{\omega}_k} + \frac{\partial}{\partial x_j}\left[-\bar{\rho}\widetilde{V}_{k,j}\widetilde{Y}_l + \bar{\rho}\left(\widetilde{u_j Y_k} - \tilde{u}_j\widetilde{Y}_k\right)\right] \tag{2.4}$$

where $\overline{\dot{\omega}_l}$ is the filtered species production. The terms with a tilde are mass-averaged variables and the terms with the bar are time averaged. The Wilcox $k-\omega$ turbulence model is [5]:

$$\frac{\partial\left(\rho k\right)}{\partial t} + \frac{\partial\left(\rho u_j k\right)}{\partial x_j} = P - \beta^*\rho\omega k + \frac{\partial}{\partial x_j}\left[\left(\mu + \sigma_k\frac{\rho k}{\omega}\right)\frac{\partial k}{\partial x_j}\right] \tag{2.5}$$

$$\frac{\partial\left(\rho\omega\right)}{\partial t} + \frac{\partial\left(\rho u_j \omega\right)}{\partial x_j} = \frac{\gamma\omega}{k}P - \beta\rho\omega^2 + \frac{\partial}{\partial x_j}\left[\left(\mu + \sigma_\omega\frac{\rho k}{\omega}\right)\frac{\partial \omega}{\partial x_j}\right] + \frac{\rho\sigma_d}{\omega}\frac{\partial k}{\partial x_j}\frac{\partial \omega}{\partial x_j} \tag{2.6}$$

These are the equations used in GEMS (ref: Section 1.3). The filtered species production term is closed using the LEM sub-grid model and is described in the following sections.

2.2 Introduction of LEM

LEM implements a one-dimensional form of the species mass fraction and energy conservation equations to describe advection, molecular diffusion, and the production of species in the sub-grid of an LES domain. LEM is implemented as a multi-scale approach by solving the species and energy equations at both the resolved and unresolved scales. A unique feature of the LEM model is that the sub-grid equations are represented by a one-dimensional set of equations. While diffusion and reaction are solved by resolving down to the Kolmogorov scales, sub-grid advection is modeled using a mapping process that simulates turbulence along a one-dimensional domain [10, 11].

The effect of eddies smaller than the LES filter width, $\bar{\Delta}$, is not captured in the resolved scale. In the LEM model they are accounted for in the sub-grid stirring term, F_{stir}. The model is a rearrangement process called a triplet map that simulates the effect of a turbulent eddy passing through a one-dimensional scalar profile, as seen in Figure 2.1. This process can be viewed as an instantaneous event that compresses the scalar's spatial profile (Fig. 2.2a) to one-third of its original size (Fig. 2.2b). The compressed profile is then replicated twice to fill the remaining domain (Fig. 2.2d). To conserve mass and energy, the center segment is inverted (Fig. 2.2c). The triplet map is implemented using three parameters: the local eddy size, ℓ, the frequency, f, and the stirring location, s_0. The eddy size and location are the same for all species and temperature profiles during a single time step so that the model remains physically consistent.

2.3 Derivation of the LEM Equations

In LEM, the energy and species equations are solved in the sub-grid on a one-dimensional line with a spatial resolution commensurate with the Kolmogorov scale. This model captures turbulent-chemistry interaction by modeling the molecular diffusion, advection, and the production of species in the sub-grid. The traditional equations for species and energy conservation are modified to enable this process. The details of these equations are given in the subsequent subsections.

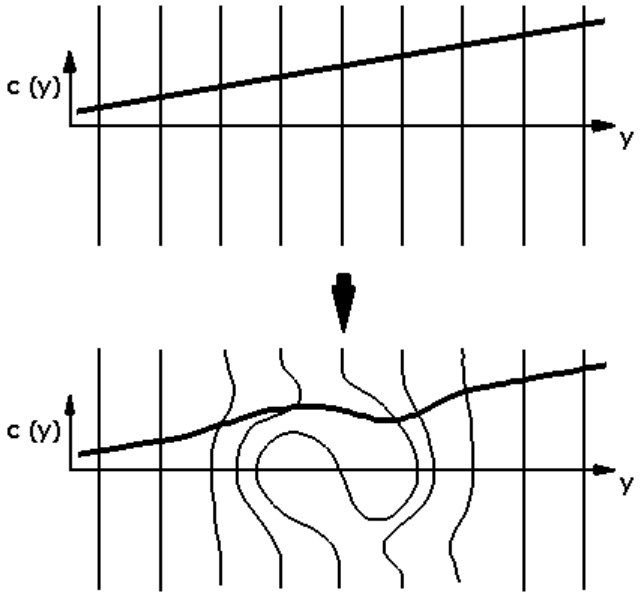

Figure 2.1: Turbulent eddy acting on scalar profile. Adapted from [10].

2.3.1 Sub-Grid Species Equation

The quantities of interest are in the sub-grid, therefore it is appropriate to work with the unfiltered conservation equations. The unfiltered species equation is

$$\frac{\partial(\rho Y_k)}{\partial t} + \frac{\partial}{\partial x_j}(\rho u_j Y_k) = -\frac{\partial}{\partial x_j}(\rho V_{j,k} Y_k) + \dot{\omega}_k \tag{2.7}$$

where $V_{j,k}$ is the diffusion velocity and $\dot{\omega}_k$ is the species production term. The advection velocity term, u_j, is split into two terms

$$u_j = \tilde{u} + u'' \tag{2.8}$$

where $\tilde{u}$ is the filtered velocity used at the resolved scale and neglected from the sub-grid equation. The u'' term represents eddies at the unresolved scale and it is therefore used in the LEM species sub-grid equation

$$\frac{\partial(\rho Y_k)}{\partial t} + \frac{\partial}{\partial x_j}\left(\rho u'' Y_k\right) = -\frac{\partial}{\partial x_j}(\rho V_{j,k} Y_k) + \dot{\omega}_k \tag{2.9}$$

Equation 2.9 represents the sub-grid species equation and is solved along the LEM line. The diffusion velocity in this equation is modeled using Fick's Law of diffusion with the Hirschfelder and Curtiss approximation for mass diffusivity

$$V_{j,k} Y_k = -\frac{D_{k,M}}{W_{mix}} \frac{\partial}{\partial x_j}(W_{mix} Y_k) \tag{2.10}$$

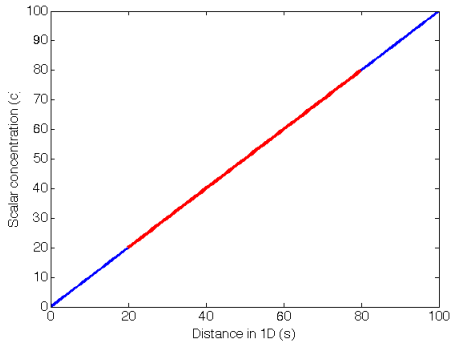

(a) Initial profile.

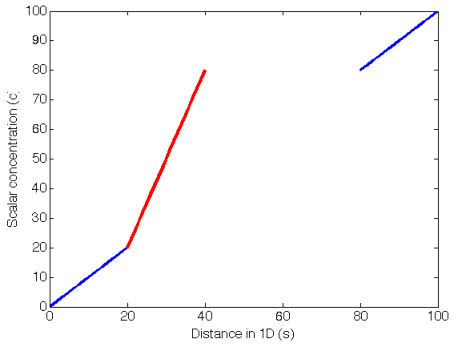

(b) Profile compressed to 1/3 of length.

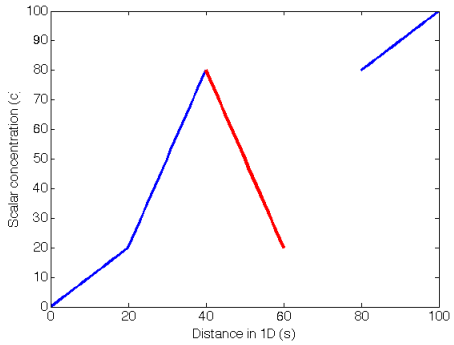

(c) Reverse of compressed profile.

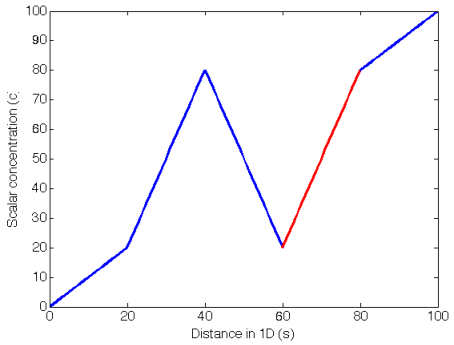

(d) Three compressed profiles.

Figure 2.2: The triplet map process is shown here. The original scalar profile (a) is compressed to one-third of the original length (b), the compressed profile is mirrored (c), and a third compressed profile is added to complete the mapping process (d).

and results in the following

$$\frac{\partial \left(\rho Y_k\right)}{\partial t} = -\frac{\partial}{\partial x_j}\left(\rho u'' Y_k\right) + \frac{\partial}{\partial x_j}\left(\rho \frac{D_{k,M}}{W_{mix}} \frac{\partial}{\partial x_j}\left(W_{mix} Y_k\right)\right) + \dot{\omega}_k \tag{2.11}$$

This equation is only correct for binary diffusion. For more than two species it is only an approximation which can lead to errors in mass conservation. To eliminate these errors a correction velocity, V_j^c, is introduced. The final form of the species equation being solved in LEM is

$$\frac{\partial Y_k}{\partial t} = \underbrace{F_{stir}}_{\text{stirring}} + \underbrace{\frac{1}{\rho}\frac{\partial}{\partial x_j}\left(\rho\left(\frac{D_{k,M}}{W_{mix}}\frac{\partial}{\partial x_j}\left(W_{mix} Y_k\right) - V_j^c Y_k\right)\right)}_{\text{diffusion}} + \underbrace{\frac{\dot{\omega}_k}{\rho}}_{\text{production}} \tag{2.12}$$

where F_{stir} is a model term to account for the effect of the sub-grid eddies. The correction velocity is defined as

$$V_j^c = \sum_{k=1}^{Ns} \frac{D_{k,M}}{W_{mix}} \frac{\partial}{\partial x_j} \left(W_{mix} Y_k \right) \tag{2.13}$$

for N_s species comprising the mixture. The prime notation has been dropped for simplicity.

2.3.2 Sub-Grid Temperature Equation

The unfiltered energy equation with no body forces and no heat addition for a calorically perfect gas is

$$\frac{\partial \rho h_0}{\partial t} + \frac{\partial}{\partial x_j} \left(\rho u_j h_0 \right) = \frac{\partial p}{\partial t} - \frac{\partial q_i}{\partial x_i} + \frac{\partial}{\partial x_j} \left(\tau_{ij} u_i \right) \tag{2.14}$$

where the term q_i is the enthalpy flux. As before the velocity can be decomposed into an filtered value (resolved) and a fluctuating component (sub-grid). The resolved scale velocity is neglected from the sub-grid equations and the fluctuating component is used.

The equation is written in terms of temperature [7], which results in the LEM energy equation

$$\rho C_{p,mix} \frac{\partial T}{\partial t} + C_{p,mix} \frac{\partial}{\partial x_j} \left(\bar{\rho} u'' T \right) = \frac{\partial}{\partial x_j} \left(\lambda \frac{\partial T}{\partial x_j} \right) - \bar{\rho} \frac{\partial T}{\partial x_j} \left(\sum_{k=1}^{Ns} C_{p,k} Y_k V_{k,j} \right) + \dot{\omega}_T \tag{2.15}$$

where λ is the thermal conductivity and $\dot{\omega}_T$ is the energy addition due to combustion given by,

$$\dot{\omega}_T = - \sum_{k=1}^{Ns} h_{s,k} \dot{\omega}_k - \sum_{k=1}^{Ns} \Delta h_{f,k}^0 \dot{\omega}_k \tag{2.16}$$

where $h_{s,k}$ is the sensible enthalpy and $h_{f,k}$ is the heat of formation. As is done for the species equations, the advection term will be modeled using a triplet map and Fick's Law for diffusion is implemented for the diffusion velocity. The final form of the energy equation is

$$\begin{aligned} \frac{\partial T}{\partial t} = & \underbrace{F_{T,stir}}_{\text{stirring}} + \underbrace{\frac{\dot{\omega}_T}{\rho C_{p,mix}}}_{\text{heat release}} \\ & + \underbrace{\frac{1}{\rho C_{p,mix}} \left(\frac{\partial}{\partial x_j} \left(\lambda \frac{\partial T}{\partial x_j} \right) + \rho \frac{\partial T}{\partial x_j} \left(\sum_{k=1}^{Ns} C_{p,k} \frac{D_{k,M}}{W_{mix}} \frac{\partial}{\partial x_j} \left(W_{mix} Y_k \right) \right) \right)}_{\text{diffusion}} \end{aligned} \tag{2.17}$$

where $F_{\text{T,stir}}$ is a model term to account for the effect of the sub-grid eddies.

2.4 Implementation of LEM

LEM embeds a one-dimensional line within a multi-dimensional LES grid. The LEM line should be oriented so that it captures the important flow features within each LES cell. In other LEM implementations the line is typically oriented to align with the maximum species mass fraction gradient [10]. For this work the LEM line is instead oriented across the flame front which can be detected by examining the temperature gradient, as described in section 2.4.2. This means that the orientation of the line will be different in each LES cell. The final equations are then written in terms of the parameterized spatial coordinate, s, and are given as

$$\frac{\partial Y_k}{\partial t} = F_{stir} + \frac{1}{\rho}\frac{\partial}{\partial s}\left(\rho\left(\frac{D_{k,M}}{W_{mix}}\frac{\partial}{\partial s}\left(W_{mix}Y_k\right) - V_j^c Y_k\right)\right) + \frac{\dot{\omega}_k}{\rho} \tag{2.18}$$

$$\frac{\partial T}{\partial t} = F_{T,stir} + \frac{\dot{\omega}_T}{\rho C_{p,mix}} + \frac{1}{\rho C_{p,mix}}\left(\frac{\partial}{\partial s}\left(\lambda\frac{\partial T}{\partial s}\right) + \rho\frac{\partial T}{\partial s}\left(\sum_{k=1}^{Ns} C_{p,k}\frac{D_{k,M}}{W_{mix}}\frac{\partial}{\partial s}\left(W_{mix}Y_k\right)\right)\right) \tag{2.19}$$

2.4.1 LEM Grid

The LEM grid is a one-dimensional line that has a length equal to the LES filter width, $\bar{\Delta}$. It is important that the grid have sufficient resolution to capture turbulent effects down to the Kolmogorov scale, η. The Kolmogorov length scale is defined as [43]

$$\eta = N_\eta \bar{\Delta} Re_{\bar{\Delta}}^{-3/4} \tag{2.20}$$

where N_η is an empirical constant that is set to unity in this work. The Reynolds number is defined as

$$Re_{\bar{\Delta}} = \frac{u'\bar{\Delta}}{\nu} \tag{2.21}$$

where u' is the LES sub-grid velocity field and is defined as

$$u' = \sqrt{\frac{2}{3}k^{sgs}} \tag{2.22}$$

where k^{sgs} is the sub-grid kinetic energy obtained from the resolved scale. To resolve the Kolmogorov length scales the grid spacing, Δs, needs to be smaller than η. In practice the grid size must be three times smaller than the Kolmogorov scale in order to exactly conserve mass during the triplet mapping process. Therefore, the number of LEM cells is given by

$$N_{LEM} = 3 \cdot \text{round}\left(\frac{\bar{\Delta}}{\eta}\right) \tag{2.23}$$

The grid spacing is determined as:

$$\Delta s = \frac{\bar{\Delta}}{N_{LEM}} \tag{2.24}$$

A schematic of the LEM grid is shown below,

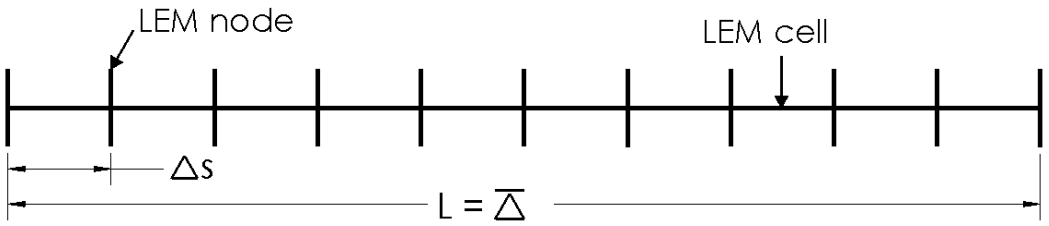

Figure 2.3: LEM grid schematic.

2.4.2 Initialization of LEM solver

In this research the LEM line is aligned with the resolved-scale temperature gradient so that the flame front is captured. This is accomplished by using the temperature gradient to determine the normal direction of the LEM line. The normal vector is dotted with the individual species gradients to obtain the species mass fractions along the line, and the temperature gradient is used to determine the temperature profile along the line. The species mass fractions, temperature, species gradients, and temperature gradient are obtained from the resolved scale (i.e. the LES solution) at the start of each LES time step.

The magnitude of the temperature gradient is calculated as follows:

$$|\nabla T| = \sqrt{\frac{\partial T}{\partial x}^2 + \frac{\partial T}{\partial y}^2 + \frac{\partial T}{\partial z}^2} \tag{2.25}$$

The species mass fraction gradients along the LEM line are determined by:

$$\nabla Y_{k,||\ \nabla T} = \frac{\nabla T}{|\nabla T|} \cdot \nabla Y_k \tag{2.26}$$

The gradients are used to linearly extrapolate the species mass fraction and temperature profiles for the LEM line using the LES value at the center of the line. However, the extrapolation process can potentially cause the species mass fraction values to be greater than unity or less than zero at the endpoints of the LEM cell. This situation occurs when a species has a zero mass fraction in one cell and the neighboring cell has a non-zero value. Any gradient in this situation will cause half

of the profile to be less than zero because the line is centered around zero. This issue is mitigated by automatically setting a zero gradient for any species that has a zero species mass fraction. In doing so, the total species mass fraction at each LEM node will no longer add up to unity, except at the center node. It is important in the initialization process that the total species over the LEM line is conserved, meaning that each nodal sum of mass fractions is unity. In order to achieve mass unity at each node it is necessary that the species gradients sum to zero as shown below:

$$\sum_{k=1}^{N_s} Y_k = 1 \tag{2.27}$$

$$\sum_{k=1}^{N_s} \frac{\partial Y_k}{\partial s} = 0 \tag{2.28}$$

In order to meet the requirement of equation 2.28 the gradients need to be adjusted to account for any species gradient that was set to zero due to zero mass fraction. The largest species value of the remaining species is adjusted so that the species gradients sum to zero as shown

$$\nabla Y_{max\ species} = -\left[\sum_{k=1}^{N_s} (\nabla Y_k) - \nabla Y_{max\ species}\right] \tag{2.29}$$

An additional issue that can arise is when one LES cell has a small non-zero species mass value and the neighboring cell has a larger value that will cause the profile to go below zero when the profile is linearly extrapolated. In this case the gradient of the species with the small mass fraction could again be set to zero but that would unnecessarily eliminate the gradient completely. Instead, all of the gradients are equally scaled so that any species that contains negative mass fractions within the profile is adjusted to have a minimum value of zero at the furthest node along the line. All of the species gradient are multiplied by a scaling factor as shown

$$\nabla Y = \nabla Y \left[\frac{\frac{2Y_{min}}{\Delta}}{\nabla Y_{min}}\right] \tag{2.30}$$

This method meets the requirements of equations 2.27 and 2.28 while maintaining as much of the original gradients as possible. A similar scaling process is applied to the temperature.

To illustrate this process, the initial species mass fraction profiles for an arbitrary four species fluid are considered. Figure 2.4 shows two cells with their corresponding species mass fractions and temperature values that were calculated at the resolved scale. The first step of the initialization process of the left cell aligns the LEM line with the maximum temperature gradient and calculates the species mass fraction gradients along this line. These gradients are used to linearly extrapolate

the species profiles for the sub-grid LEM and are shown in Figure 2.5a. From the plot it can be seen that both Y_3 and Y_4 have negative species mass fraction values for a portion of their profiles. Since Y_4 has a value of zero at the cell center, as shown in Figure 2.4, the gradient must be zero to avoid a negative mass fraction. Additionally, the gradient for Y_1 is modified so that the sum of the gradients add up to zero per equation 2.28. Species Y_3 has a non-zero value at the cell center but the gradient is large enough such that a negative species mass fraction will exist at the extent of the domain. This issue is mitigated by scaling all the profiles so that Y_3 is zero at the far left node. Figure 2.5b shows the final initial profile for this LEM line.

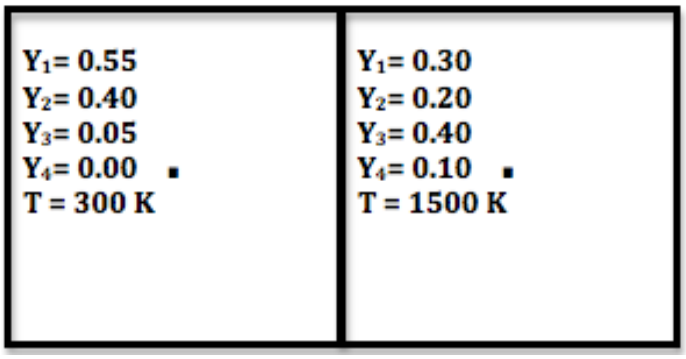

Figure 2.4: Adjacent LES cells with their corresponding mass fractions and temperature.

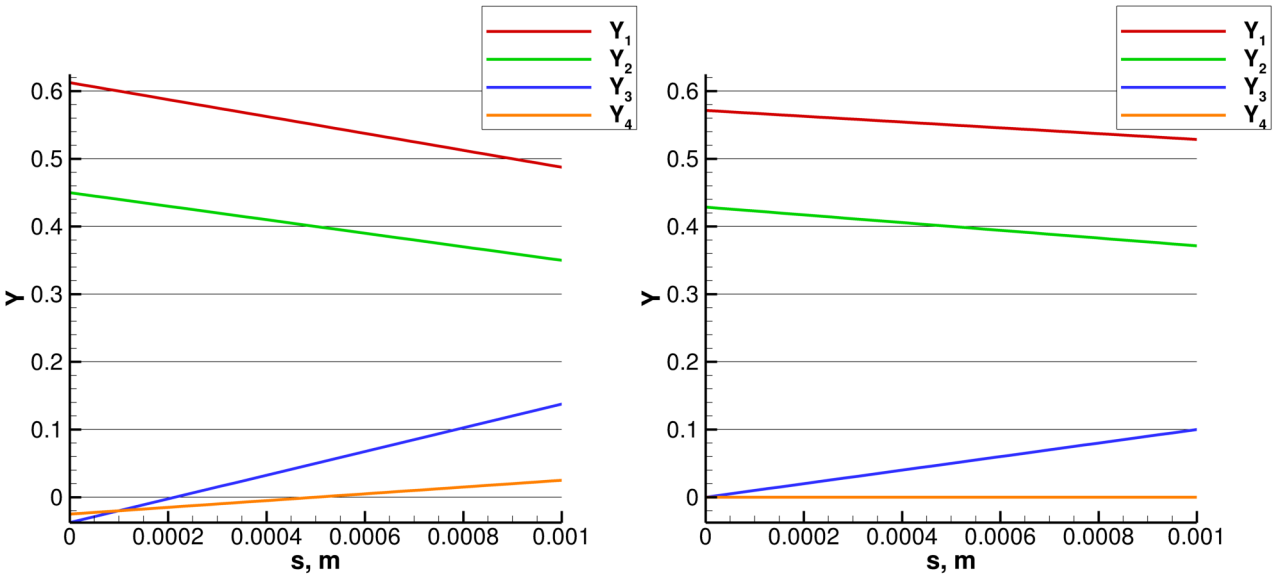

(a) Initial species mass fraction along a LEM line with negative mass on the left side.

(b) Re-scaled species mass fraction along a LEM line without negative mass.

Figure 2.5: Initialization process along LEM line.

2.4.3 Numerical Implementation of LEM Processes

In practice equations 2.18 and 2.19 are solved in three explicit steps, with each step corresponding to the diffusion, production, and stirring. The LEM equations are,

$$\frac{\partial Y_k}{\partial t} = F_{stir} + \frac{1}{\rho}\frac{\partial}{\partial s}\left(\rho\left(\frac{D_{k,M}}{W_{mix}}\frac{\partial}{\partial s}\left(W_{mix}Y_k\right) - V_j^c Y_k\right)\right) + \frac{\dot{\omega}_k}{\rho} \tag{2.31}$$

$$\frac{\partial T}{\partial t} = F_{T,stir} + \frac{1}{\rho C_{p,mix}}\left(\frac{\partial}{\partial s}\left(\lambda\frac{\partial T}{\partial s}\right) + \rho\frac{\partial T}{\partial s}\left(\sum_{k=1}^{Ns} C_{p,k}\frac{D_{k,M}}{W_{mix}}\frac{\partial}{\partial s}\left(W_{mix}Y_k\right)\right)\right) + \frac{\dot{\omega}_T}{\rho C_{p,mix}} \tag{2.32}$$

The species production equations are,

$$\frac{\partial Y_k}{\partial t} = \frac{\dot{\omega}_k}{\rho} \tag{2.33}$$

$$\frac{\partial T}{\partial t} = \frac{\dot{\omega}_T}{\rho C_{p,mix}} \tag{2.34}$$

An ODE solver is implemented to advance equations 2.33 and 2.34 in time because the chemical time scales can be very small. The stirring process is an instantaneous rearrangement event (detailed in section 2.2) and therefore no ODE is necessary.

The LEM solution is advanced to the LES physical time step by a sub-grid time step interval of Δt, as seen in Figure 2.6. The value of Δt is determined as the minimum of the stirring or diffusion time steps (ref. sections 2.4.3.1 and 2.4.3.2). In practice Δt typically corresponds to the stirring time step because it is smaller than the diffusion time step.

The combustion equations 2.33 and 2.34 are simultaneously integrated over an interval of Δt using an ODE solver. Next, the updated solution is instantaneous stirred using the triplet map rearrangement process. Finally, the diffusion is advanced by Δt using a finite difference scheme which smooths out the sharp edges from the stirring. This process is repeated until the LEM solution has matched the LES interval, with a partial step implemented at the end as needed.

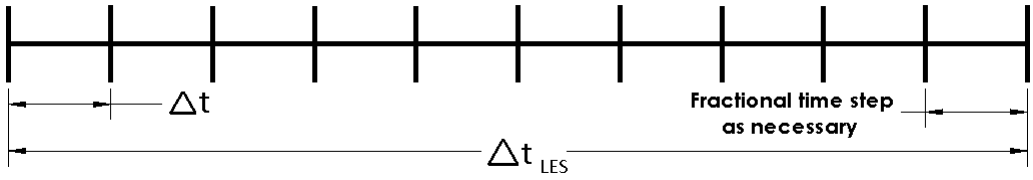

Figure 2.6: LEM time stepping schematic.

2.4.3.1 Stirring

The stirring is implemented using three parameters: the local eddy size, ℓ, the frequency, f, and the stirring location, s_0. The eddy size is chosen randomly from a probability density function (PDF), $f(\ell)$, in the range of $\bar{\Delta}$ to η. The eddy size PDF is:

$$f(\ell) = \frac{\frac{5}{3}\ell^{-8/3}}{\eta^{-5/3} - \bar{\Delta}^{-5/3}} \tag{2.35}$$

This PDF is integrated to obtain a cumulative distribution function (CDF). Enforcing the condition that the CDF takes a value of unity when $\ell = \bar{\Delta}$ results in the following,

$$\ell = \left[CDF\left(\bar{\Delta}^{-5/3} - \eta^{-5/3}\right) + \eta^{-5/3}\right] \tag{2.36}$$

The length of the eddy for each time step is obtained by choosing a random number for the CDF value in equation 2.36. The stirring frequency, f, is calculated as:

$$f = \frac{54}{5}\frac{\nu Re_{\bar{\Delta}}}{C_\lambda \bar{\Delta}^3}\frac{\left[(\bar{\Delta}/\eta)^{5/3} - 1\right]}{1 - (\bar{\Delta}/\eta)^{4/3}} \tag{2.37}$$

where C_λ is a constant determined to be 0.067 [16]. This value is then used to calculate the stirring time step as follows:

$$\Delta t_{stir} = \frac{1}{f\bar{\Delta}} \tag{2.38}$$

Once the eddy size is calculated it is then possible to determine the location of the stirring event. The location is chosen using a random number generator, assuming an initial distribution, with the requirement that the whole eddy length, ℓ, must to fit on within the domain. This is accomplished by putting a restriction that the node at which the event occurs must be less than $N_{\text{LEM}} - \ell$. Once the eddy length and location are determined, the triplet map can then be applied to the scalar (species mass fraction and temperature) profile. The triplet map rearranges the profile as follows:

$$\phi(s) \rightarrow \phi(M(s)) \tag{2.39}$$

where the scalar value is mapped to the one-dimensional coordinate, s, and $M(s)$ is the mapping [24] which is defined by:

$$M(s) = s_0 + \begin{cases} 3\ (s - s_0) & \text{if} \quad s_0 \leq s \leq s_0 + 1/3\ \ell \\ 2\ \ell\ \text{-}\ 3(s - s_0) & \text{if} \quad s_0 + 1/3\ell \leq s \leq s_0 + 2/3\ \ell \\ 3(s - s_0) - 2\ell & \text{if} \quad s_0 + 2/3\ell \leq s \leq s_0 + \ell \\ s\ \text{-}\ s_0 & \text{if} \quad \text{otherwise} \end{cases}$$

2.4.3.2 Diffusion

The diffusion equations in LEM are solved using forward Euler in time and second-order central differencing in space. The equations are:

$$\frac{\partial Y_k}{\partial t} = \frac{1}{\rho}\frac{\partial}{\partial s}\left(\rho\left(\frac{D_{k,M}}{W_{mix}}\frac{\partial}{\partial s}\left(W_{mix}Y_k\right) - V_j^c Y_k\right)\right) \tag{2.40}$$

$$\frac{\partial T}{\partial t} = \frac{1}{\rho C_{p,mix}}\left(\frac{\partial}{\partial s}\left(\lambda\frac{\partial T}{\partial s}\right) + \rho\frac{\partial T}{\partial s}\left(\sum_{k=1}^{Ns} C_{p,k}\frac{D_{k,M}}{W_{mix}}\frac{\partial}{\partial s}\left(W_{mix}Y_k\right)\right)\right) \tag{2.41}$$

The derivatives in the above equations are evaluated using central differencing stencil as shown:

$$\frac{\partial \phi}{\partial s} = \frac{\phi_{i+1} - \phi_{i-1}}{2\Delta s} \tag{2.42}$$

A Neumann boundary condition $\left(\frac{\partial \phi}{\partial s} = 0\right)$ is implemented as:

$$\frac{\partial \phi}{\partial s} = \frac{-3\phi_1 + 4\phi_2 - \phi_3}{2\Delta s} = 0 \Rightarrow \phi_1 = \frac{4\phi_2 - \phi_3}{3} \tag{2.43}$$

$$\frac{\partial \phi}{\partial s} = \frac{3\phi_{N_{LEM}+1} - 4\phi_{N_{LEM}} + \phi_{N_{LEM}-1}}{2\Delta s} = 0 \Rightarrow \phi_{N_{LEM}+1} = \frac{4\phi_{N_{LEM}} - \phi_{N_{LEM}-1}}{3} \tag{2.44}$$

The time step for diffusion is chosen as

$$\Delta \mathrm{t}_{\mathrm{diff}} = VNN \frac{\Delta s^2}{\max\left(D, \frac{\lambda}{\rho C_{p,mix}}\right)} \tag{2.45}$$

where VNN is set at 0.5 for numerical stability.

2.4.3.3 Combustion

The change in species mass fraction and temperature due to combustion is calculated by the following ODE's

$$\frac{\partial Y_k}{\partial t} = \frac{\dot{\omega}_k}{\rho} \tag{2.46}$$

$$\frac{\partial T}{\partial t} = \frac{\dot{\omega}_T}{\rho C_{p,mix}} \tag{2.47}$$

The production rate for each species is expressed as:

$$\dot{\omega}_k = W_k \sum_{j=1}^{M} \left(\nu'_{k,j} - \nu''_{k,j}\right) w_j \tag{2.48}$$

where M is the number of reactions, W_k is the molecular weight, $\nu'_{k,j}$ and $\nu''_{k,j}$ are the stoichiometric coefficients of the reactants and products, respectively, and w_j is the progress rate variable. The progess rate variable can be calculated for global reactions, equilibrium reactions, Lindemann falloff reactions, third body reactions, troe reactions and Tsang-Herron reactions. The ODE's are solved using the solver, DVODE, which uses implicit Adams method to solve equations (2.46) and (2.47).

2.4.4 Filtered Species Production Term

The LEM solution advances the stirring, diffusion, and species production to the next physical time step, Δt_{LES}, for the entire LEM line. The filtered species production term for each species is calculated by determining the average species production over the entire LEM line as follows,

$$\overline{\dot{\omega}}_k = \frac{1}{N_{\mathrm{LEM}} + 1} \sum_{i=1}^{N_{\mathrm{LEM}}+1} \dot{\omega}_{k,i} \tag{2.49}$$

where k represents each individual species.

2.5 Comparison to Past Work

This approach uses LEM to obtain the filtered species production term in the large scale species mass fraction equations 2.4. Previous work did not solve the Eulerian form of the species equations at the resolved scale [43]. Instead, the species mass fraction is accounted for by a Lagrangian splicing method in which mass is transferred between LEM lines using a large scale advection approach as discussed in section 1.1.3. The large scale advection is an *ad hoc* process that arbitrarily transfers mass between LES cells accounting only for advection, while neglecting diffusion. The benefit of the current approach is that the LEM solution contributes to the full multi-dimensional species equations at the resolved scale, which includes a consistent form of the resolved scale convection and diffusion.

2.6 Assumptions and Limitations of LEM

At this point it is important to explicitly state the assumptions that were used in deriving the species transport and temperature equations to better understand the limitations of LEM. A salient feature of the LEM approach is that a one-dimensional line is embedded within a multi-dimensional domain. It is aligned with the maximum temperature gradient in order to capture the flame front, however, it is not able to capture all of the relevant flow properties that would be captured by a three-dimensional DNS. Second, the form of the energy equation used in LEM assumes that there is a constant pressure within the LES cell from one physical time step to the next. This makes LEM appropriate for deflagarations but is not correct in areas where compressibility effects are important, such as detonations or acoustics coupling. Third, there are two separate temperatures calculated because an energy equation is solved at both the resolved and unresolved scales. The temperature obtained from LEM is discarded at the end of each physical time step since it is more approximate. Additionally, a no flux boundary condition is applied to the LEM line so there is no transfer of mass between LEM lines through diffusion or advection. Lastly, in areas where the LES grid spacing approaches the Kolmogorov scales, the LEM grid will reduce to a single node or a few nodes. In this limit, this LEM approach will naturally reduce to a laminar combustion source term closure which is the correct DNS limit.

CHAPTER 3

Stand-Alone LEM Implementation

The LEM equations are solved in three explicit processes, which includes stirring, diffusion and combustion. It is crucial that all of these process are conservative so that the LEM model is physically accurate. This chapter tests the predictions of the LEM model for a single sub-grid line and then focuses on verifying that the model for the three processes. In addition, the energy spectrum is calculated in order to verify that LEM can accurately represent turbulent statistics in the inertial sub-range.

3.1 Stirring

The stand-alone sub-grid stirring process, as described in section 3.3.3.1, is tested using four species distributed along a 36 cell LEM line. The cell centered species mass fraction values for Y_1, Y_2, Y_3, and Y_4 are 0.4, 0.3, 0.2, and 0.1, respectively, which could represent mass fractions of oxidizer, products, and fuel, for example. An equal and opposite gradient is applied to species Y_1 and Y_2, similar to Y_3 and Y_4, so that the total species mass fraction within the domain adds to unity at each LEM node, as seen in Figure 3.1a. Additionally, a cell centered temperature value of 300 K is extrapolated to created a temperature gradient within the domain, and is shown in Figure 3.1b. A single stirring event is applied at a random location along the LEM line (ref: Figures 3.2a and 3.2b) to simulate the effect of sub-grid advection within the domain. It is worth noting that the same eddy size and location is applied to both the species mass fraction and temperature profiles so as to maintain the physical representation of an eddy acting on the sub-grid, as described in section 2.2. The single stirring event is able to conserve the scalar quantities contained in the LEM line but is important that this process remains conservative for a large number of instances.

To further test the stirring process, the code is run for one hundred stirring events (ref: Figures 3.3a and 3.3b) on the same initial profiles and the total mass of each species and temperature

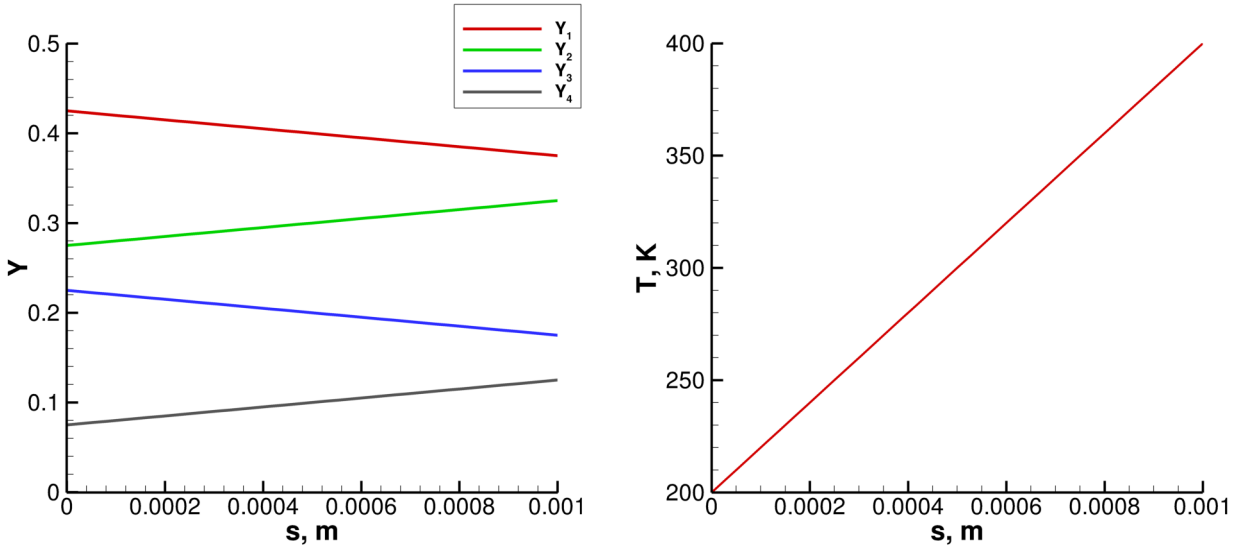

(a) Initial species mass fraction profile.

(b) Initial temperature profile.

Figure 3.1: Initial species mass fraction and temperature distribution for a single LEM line.

contained within the LEM line is calculated before and after the stirring using a trapezoidal rule, as shown in Table 3.1. The results in the table show that both the species mass fraction and temperature quantities are conserved for a large number of stirring events, which verifies that the stirring process is correctly implemented. In practice, a typical LES time step will only have a handful of sub-grid stirring events which means that this test far exceeds the number of stirring events that would be applied during a given simulation.

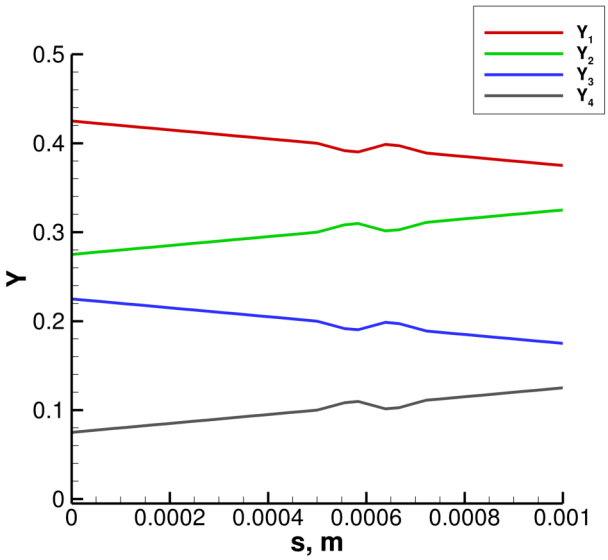

(a) Single stirring event applied to the species mass fraction profiles.

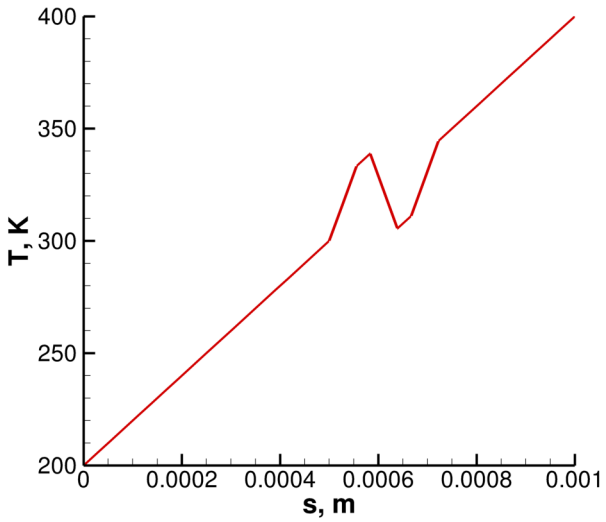

(b) Single stirring event applied to the temperature profile.

Figure 3.2: Single stirring event applied to the species mass fraction and temperature profiles.

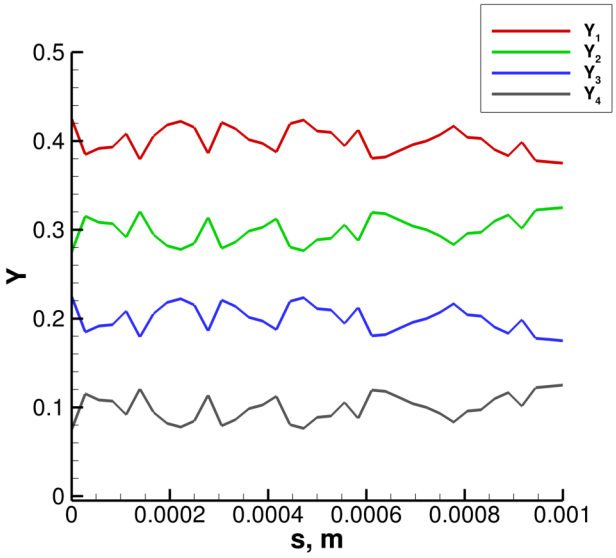

(a) One hundred stirring event applied to the species mass fraction profiles.

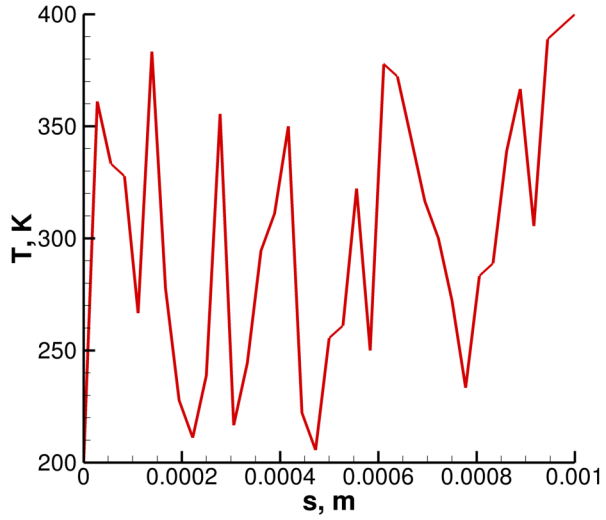

(b) One hundred stirring event applied to temperature profile.

Figure 3.3: One-hundred stirring events applied to the species mass fraction and temperature profiles.

Table 3.1: Area before and after 100 stirring events

Variable	Area Before Stirring	Area After Stirring
Y_1	4.00 x10^{-4}	4.00 x10^{-4}
Y_2	3.00 x10^{-4}	3.00 x10^{-4}
Y_3	2.00 x10^{-4}	2.00 x10^{-4}
Y_4	1.00 x10^{-4}	1.00 x10^{-4}
total mass	1.00 x10^{-3}	1.00 x10^{-3}
$T(K)$	300.0	300.0

3.2 Diffusion

The diffusion process, as described in Section 2.4.3.2, is tested using four species distributed along a 36 cell LEM line. The same initial distributions as the previous section are used here and are again shown in Figures 3.4a and 3.4b. The diffusion process is run with a Neumann boundary condition for a total of 200 ms which corresponds to around 200 K time steps. The no-flux boundary condition is implemented so the total mass and temperature contained within the LEM line is conserved.

The diffused profiles are shown in Figures 3.5a and 3.5b and it can be seen that all the profiles have dissipated close to the nominal values, as expected. The quantity of species and the temperature contained in the domain is calculated before and after the diffusion process using a trapezoidal rule and are shown in Table 3.2. The tabulated results show that the diffusion process has accumulated error that varies between 1% and 3% of the expected values. This error is due to the second order finite difference scheme that is used to represent the spatial gradient and eliminating this error completely is unavoidable. However, in practice the diffusion will take place for a much shorter amount of time and for fewer time steps than in this test, so the accumulated error with this process will be minimized in a given simulation.

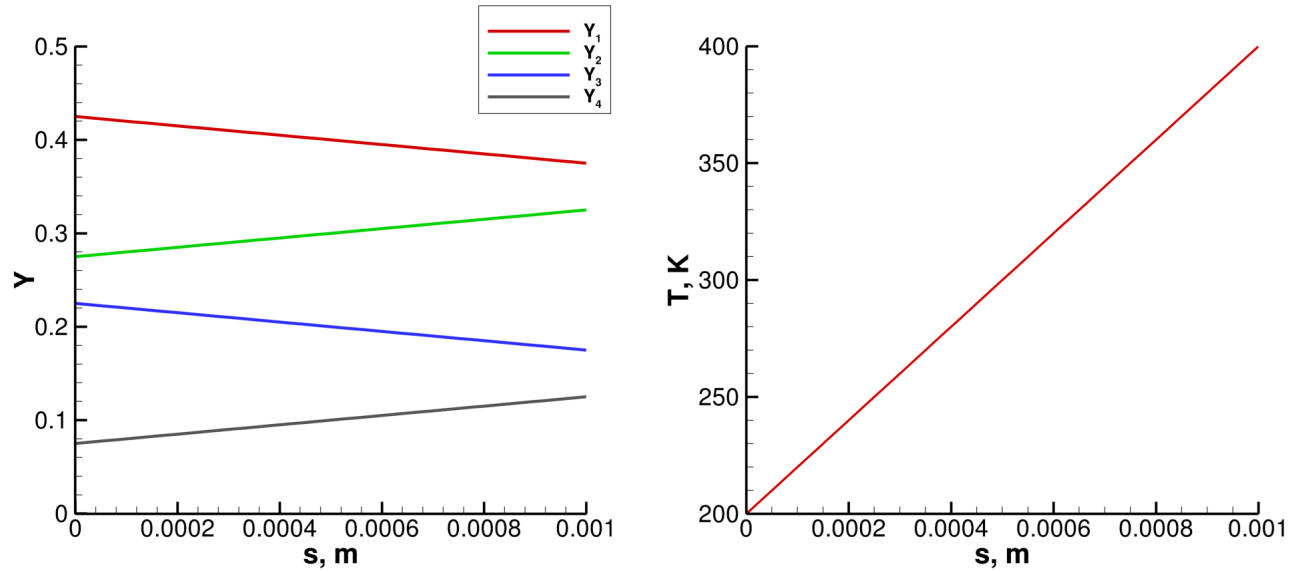

(a) Initial species mass fraction profile.

(b) Initial temperature profile.

Figure 3.4: Initial species mass fraction and temperature distribution for a single LEM line.

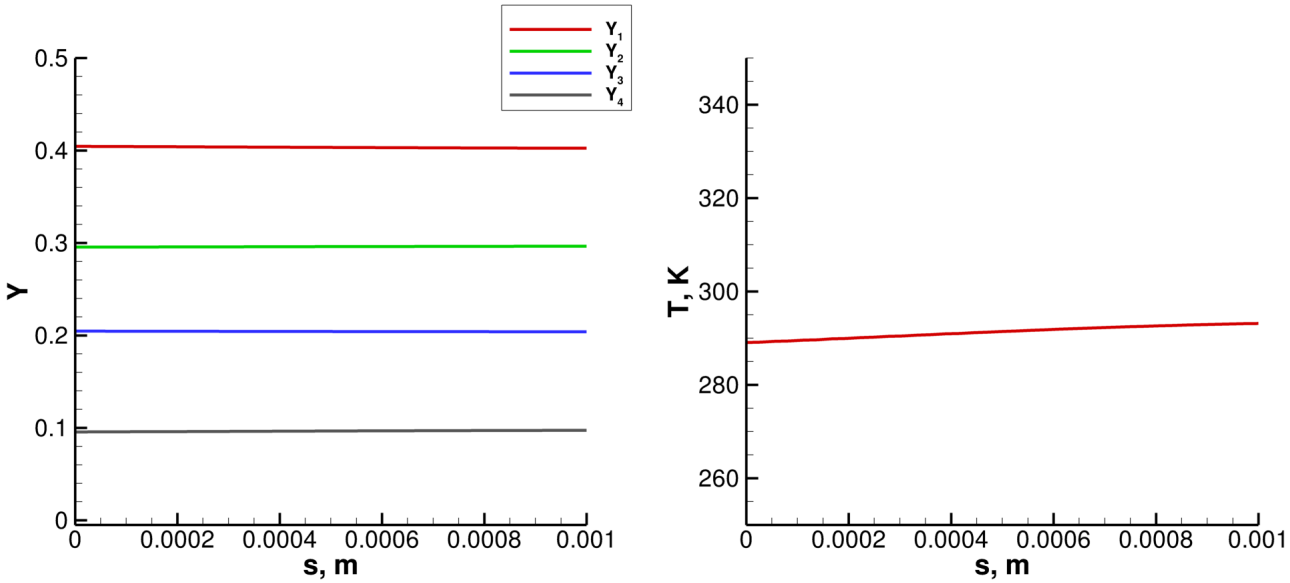

(a) Diffused species mass fraction profiles.

(b) Diffused temperature profile.

Figure 3.5: Diffusion process applied to the species mass fraction and temperature profiles.

Table 3.2: Area before and after diffusion.

Variable	Area Before Diffusion	Area After Diffusion
Y_1	4.00 x10^{-4}	4.03 x10^{-4}
Y_2	3.00 x10^{-4}	2.96 x10^{-4}
Y_3	2.00 x10^{-4}	2.04 x10^{-4}
Y_4	1.00 x10^{-4}	0.97 x10^{-4}
total mass	1.00 x10^{-3}	1.00 x10^{-3}
$T(K)$	300.0	291.12

3.3 Combustion

The stand-alone combustion process was tested using GRI-Mech 1.2 [44]. GRI-Mech is an optimized detailed chemical reaction mechanism capable of the best representation of natural gas flames and ignition to date. GRI-Mech is a list of elementary chemical reactions and associated rate constant expressions. The version utilized in this work contains 177 reactions and 32 species which is commonly used because of its relatively small size and ability to accurately predict methane and air based combustion.

A simulation is run using LEM combustion and it is compared to the solution from CHEMKIN, a software tool developed by Sandia National Laboratories for solving complex chemical kinetics problems; the mechanism in GRI-Mech 1.2 was incorporated into CHEMKIN as well. The simulation is initialized with species mass fraction values of 0.504 for oxygen (O_2), 0.370 for water (H_2O), and 0.126 for methane (CH_4) at 101 kPa and 1500 K. It can be seen from Figure 3.6 that both methods achieve the same species mass fraction values for oxygen and methane but in a slightly different amount of time. The combustion temperature is compared in Figure 3.7 and again shows very good agreement in final temperature but has the same discrepancy in the reaction time. The difference in time is probably due to the lower tolerance value set in CHEMKIN compared to the LEM solver.

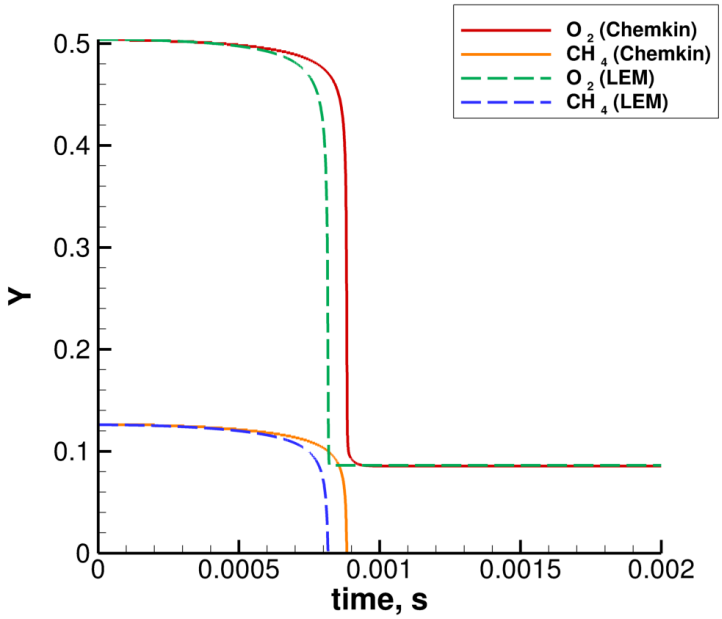

Figure 3.6: Comparison of oxygen and methane during combustion for GRI-Mech 1.2 reaction mechanism using LEM and CHEMKIN.

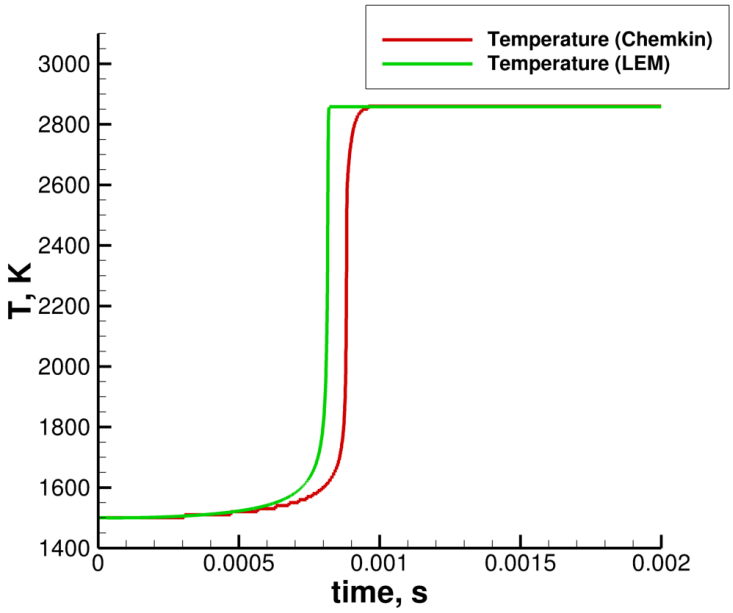

Figure 3.7: Comparison of temperature during combustion for GRI-Mech 1.2 raction mechanism using LEM and CHEMKIN.

3.4 Energy Spectrum of LEM

The kinetic energy contained in a turbulent flow cascades down from the largest to the smallest eddies. Since turbulence contains a continuous spectrum of scales, it is convenient to do analysis in terms of the spectral distribution of energy [5]. The wavenumber spectrum in turbulent flows can be divided into three sections, which are the energy containing eddies, the inertial sub-range, and the viscous range. In LES, the resolved scale captures the energy containing eddies and extends into the inertial range. The LEM sub-grid model aims to represent the inertial sub-range of a turbulent flow which extends down to the Kolmogorov length scale.

A well established property of the inertial sub-range is the Kolmogorov -5/3 law. It is important that the LEM be compared to this criterion in order to validate its viability as a turbulence model.

The energy spectrum produced by the LEM model is determined by running the full LEM solver, as described in section 2.4.3, using a single-step methane reaction that contains four different species within the domain. The stoichiometric reaction is

$$CH_4 + 2O_2 = 2H_2O + CO_2 \tag{3.1}$$

The two cases that are considered here are a 5 mm long LEM line that contains 96 LEM cells and 2 mm long LEM line that contains 120 LEM cells. These two cases are chosen because they represent possible LEM grids in practical simulations. Case 1 (5mm) has and initial cell centered species mass fraction values of 0.4, 0.3, 0.2, and 0.1 for oxygen, methane, water, and carbon dioxide, respectively. Case 2 (2mm) has the stoichiometric values of 0.8 for oxygen and 0.2 for methane, hence without the presence of product at time t=0. Both cases are run for a total of 10 μs, and the resulting stirred profiles for methane are shown in Figures 3.8 and 3.10, for case 1 and 2, respectively.

To examine the frequency content of the signal, a power spectral density analysis is performed on the final profiles. A total of 5 mm of spatial data are analyzed, with the data spaced 52 μm apart for case 1. For case 2 a total of 2 mm of spatial data are analyzed, with the data spaced 16 μm apart. The PSD results are plotted on a log scale and are shown in Figures 3.9 and 3.11, for cases 1 and 2, respectively. Both figures have an additional red line with a -5/3 slope that is used verify that the LEM turbulence does indeed represent the inertial sub-range.

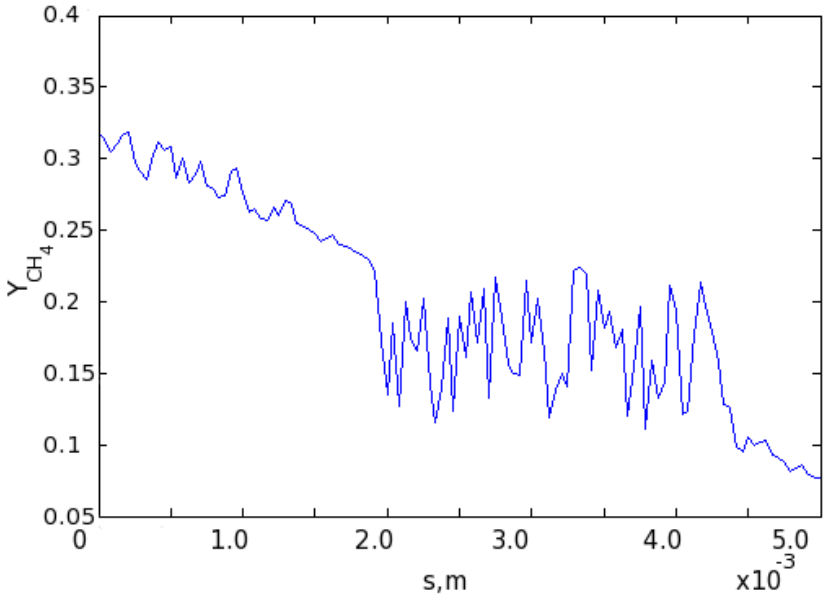

Figure 3.8: The methane profile along the 5 mm long domain after LEM has been run for 10 μs, with initial conditions corresponding to case 1.

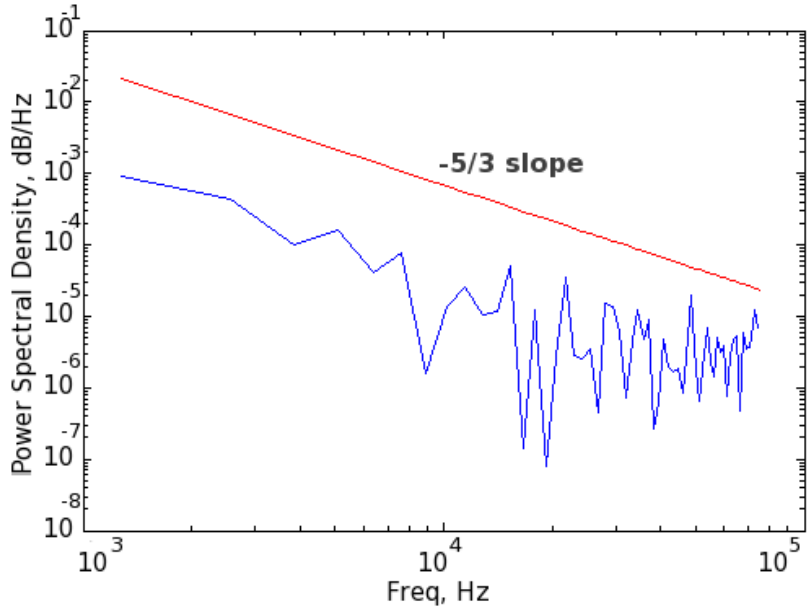

Figure 3.9: PSD of the methane profile for the 5 mm long line after LEM has been run for 10 μs, with initial conditions corresponding to case 1. The red line has a -5/3 slope that is used to verify the turbulence profile follows Kolomogorov -5/3 law.

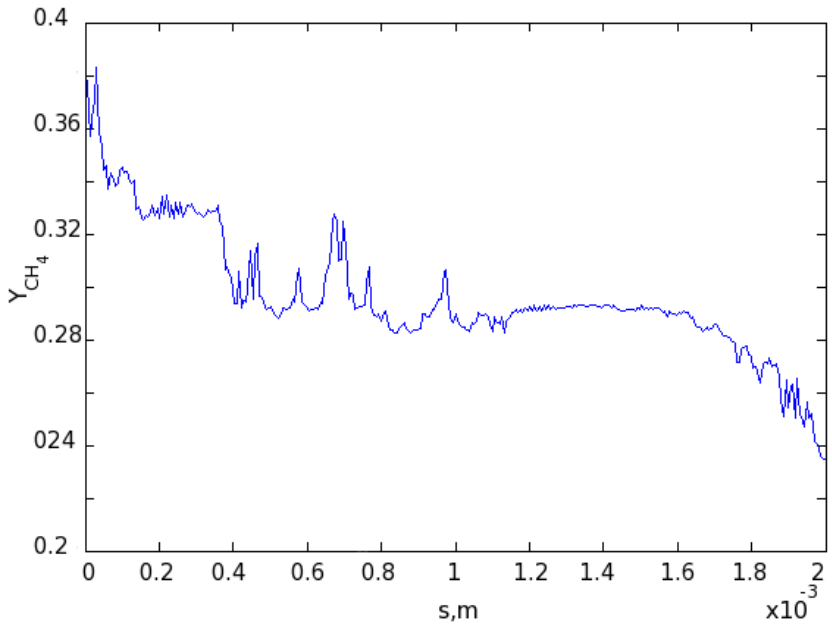

Figure 3.10: The methane profile along the 2 mm long domain after LEM has been run for 10 μs, with initial conditions corresponding to case 2.

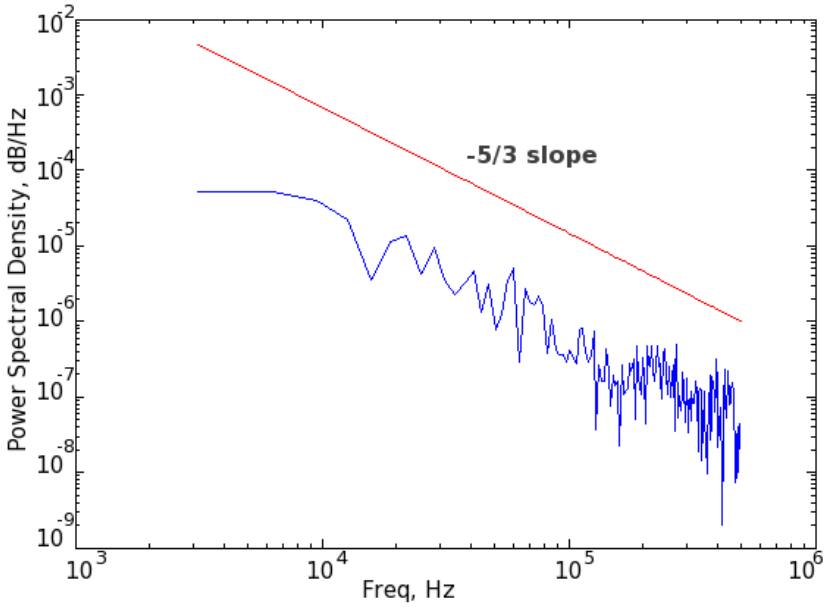

Figure 3.11: PSD of the methane profile for the 2 mm long line after LEM has been run for 10 μs, with initial conditions corresponding to case 2. The red line has a -5/3 slope that is used to verify the turbulence profile follows Kolomogorov -5/3 law.

3.5 Summary of Stand-Alone Results

The three fundamental processes of stirring, diffusion, and chemical reaction associated with LEM were tested to verify that each performs correctly. The stirring successfully implements a triplet map to produce a turbulent profile that is completely conservative. The diffusion functions as expected but produces a small error due to truncation errors on a finite mesh. The LEM combustion model was tested using the Gri-Mech reaction mechanism and produces very similar results to Chemkin, noting that the slight difference in reaction time is probably a result of the time stepping method employed in the Chemkin solver.

Additionally, a power spectral density analysis has been used to determine the energy spectrum produced by the LEM model, and the results show that applying LEM to a scalar profile produces a -5/3 slope in the energy spectrum that is expected to be seen in the inertial sub-range. These results validate LEM as a reasonable turbulence model for combustion processes. This chapter has verified that the LEM model has been properly implemented and appropriately represents turbulence in the sub-grid scale. The following chapter will couple LEM with GEMS to form the LEM-LES model. The combined solver will then be applied to a bluff-body stabilized flame.

CHAPTER 4

LEM-LES

This chapter uses the integrated LEM-LES solver to simulate reactive flow in the Volvo rig, which consists of a rectangular duct that contains an equilateral triangle-shaped bluff-body flameholder. The results for temperature, centerline axial velocity, normalized velocity, and lean blow-out equivalence ratio from the reactive LEM-LES code are compared to experimental data to assess the validity of LEM as a sub-grid model for turbulent combustion in bluff-body stabilized flames.

4.1 Volvo Rig Description

The Volvo rig was designed in the early 1990s and has been a valuable experiment for a computational comparison due to the detailed experimental data available [27, 28, 29]. The test rig is a 1.55m long rectangular duct that is 0.24m wide by 0.12m high and is fed by a choked air inlet. The rig is divided into a 0.55m inlet section and a 1.00m combustor section. The inlet section injects a choked air and fuel mixture into the duct which then travels through a honeycomb and screen before it enters the combustor section. The combustor section contains a 40mm equilateral triangular bluff body that sits 0.318m downstream from the inlet section which spans the width of the 0.24m duct and acts as a flame holder. After exiting the combustor the flow is exhausted into a large circular duct that is 0.352m in diameter. Figure 4.1 shows the geometric schematic for the Volvo test rig downstream of the honeycomb screen.

4.2 Simulation Description

The LEM-LES solver is applied to the Volvo rig geometry to compute lean blow-out, time averaged temperature, and normalized time averaged velocity. The simulation is performed in two dimensions using a mesh that contains 49,978 cells. The downstream region of the mesh is important because

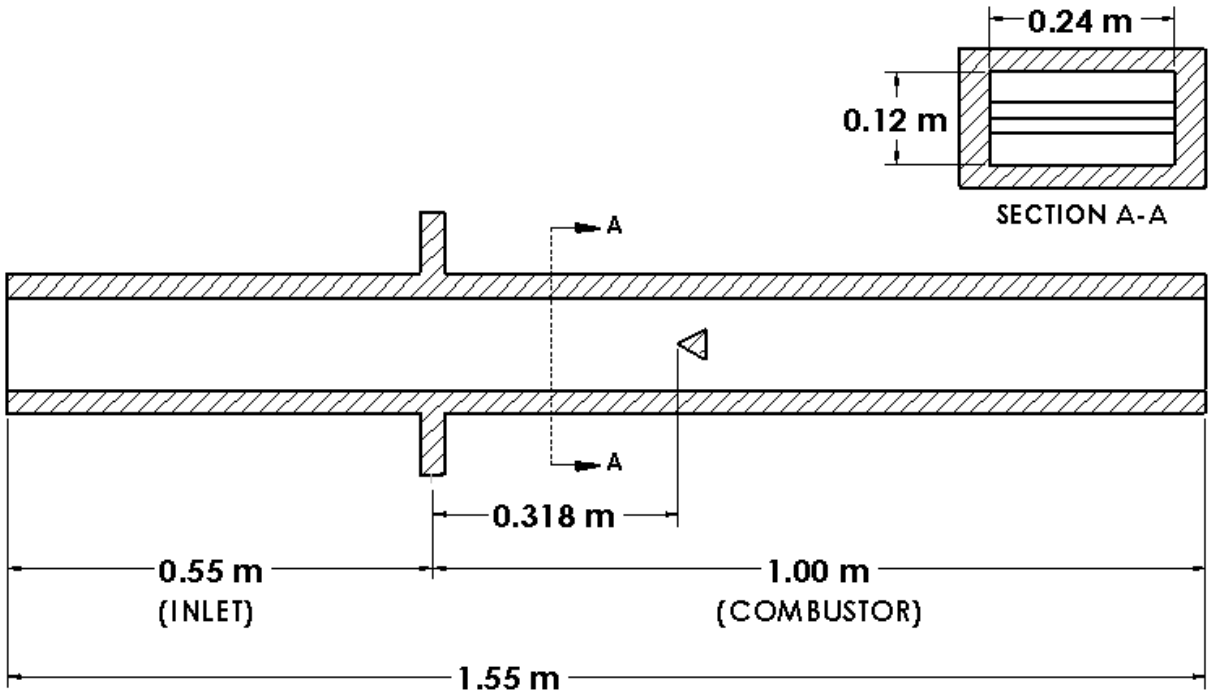

Figure 4.1: Cross-sectional view of the Volvo geometry, including the triangular flameholder.

that is where the flame resides and therefore it is important to properly capture this region. A cell width of 4mm is chosen in the axial direction downstream of the flameholder because it matches Pope's criterion in which 80% of the turbulent kinetic energy is resolved.

The inlet boundary has a mass inflow of 0.62 kg/s and a stagnation temperature of 288K. The flameholder and channel walls are treated as adiabatic, non-slip surfaces, meanwhile the exit has a fixed back pressure of 100kPa. The combustion mechanism is a global propane reaction that contains 6 species: propane (C_3H_8), oxygen (O_2), nitrogen (N_2), carbon dioxide (CO_2), water (H_2O), and neon (Ne). The simulations are run with a physical time step of $5x10^{-5}$s using both LEM-LES and a laminar closure for the combustion source term so that the results can be compared. The temperature and velocity profiles are computed for an equivalence ratio of 0.65 to compare with experimental data [28]. To predict lean blow-out, an equivalence ratio of 0.5 is chosen because that has been shown in experiments to extinguish the flame [27].

4.3 Results

4.3.1 Stable Combustion

The first simulation that is run compares laminar reactive flow code results to the LEM-LES solver with an equivalence ratio of 0.65. A single flow through time for the input parameters discussed in Section 4.2 is 0.087 seconds. The simulations were run for 0.15 and 0.25 seconds which corresponds to roughly 2 and 3 flow through times, respectively. The instantaneous temperature contour plots are shown in Figures 4.2 and 4.3 for results from the two different methods at times 0.15 and 0.25 seconds, respectively. The contour plots show that the laminar reactive flow solution achieves a temperature around 1950K downstream of the flameholder where LEM-LES predicts 1850K for the same region. A qualitative look at the instantaneous profiles shows that the contours have noticeably different flame shapes downstream of the flameholder in addition to the quantitative temperature difference. The instantaneous contour profiles can be misleading however, because the models are initialized in a non-physical manner which may result in the simulations being at different points in the combustion cycle. To ameliorate this issue an average temperature profile is useful because it will capture the whole combustion cycle throughout the simulation. The time averaged temperature shown in Figure 4.4 reveals that the downstream profile flame shapes are in-fact similar with the exception of the temperature value downstream of the flameholder, with higher temperatures for the laminar closure model persisting into the farfield.

A quantitative analysis is performed by time averaging the temperature and normalizing velocity profiles downstream of the flameholder and comparing these values to experimental data. The locations that are measured for the time averaged temperature profile are 0.15m, 0.35m, and 0.55m downstream of the flameholder. The normalized time averaged velocity is measured 0.015m and 0.15m downstream of the flameholder. In addition to the transverse velocity a normalized centerline axial velocity is measured starting from the edge of the flameholder and extending the length of the duct. The location of the measured data is shown in Figure 4.5.

The time averaged temperature profiles (Figures 4.6, 4.7, and 4.8) show that both LEM-LES and laminar combustion over-predict the temperature in all three locations. The CFD solutions furthermore become more erroneous further downstream of the flameholder. The LEM-LES based temperatures are lower at each point and are therefore closer to the experimental data than tem-

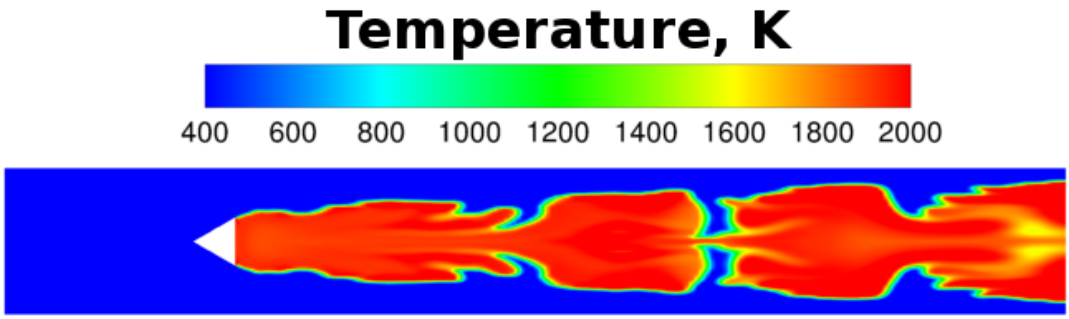

(a) Instantaneous temperature contours of laminar closure model 0.15 seconds after initialization with an equivalence ratio of 0.65.

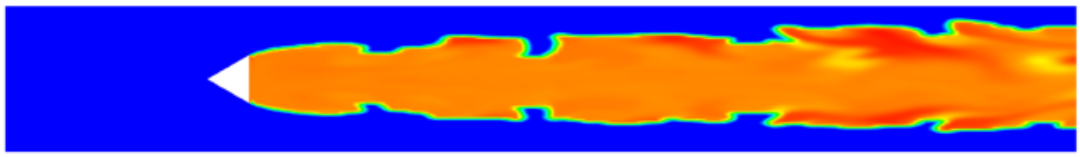

(b) Instantaneous temperature contours of LEM sub-grid model 0.15 seconds after initialization with an equivalence ratio of 0.65.

Figure 4.2: Comparison of the instantaneous temperature contours of laminar combustion to LEM sub-grid model 0.15 seconds after initialization with an equivalence ratio of 0.65.

peratures derived from the laminar reactive flow calculation. It can also be seen that both of the solutions predict the width of the flame sufficiently well but produce a steeper gradient at the fringes of the flame than is seen in the experimental data.

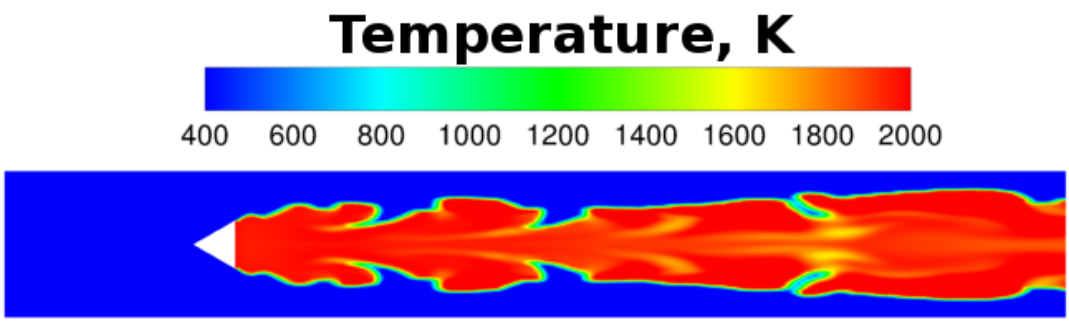

(a) Temperature contours of laminar closure model 0.25 seconds after initialization with an equivalence ratio of 0.65.

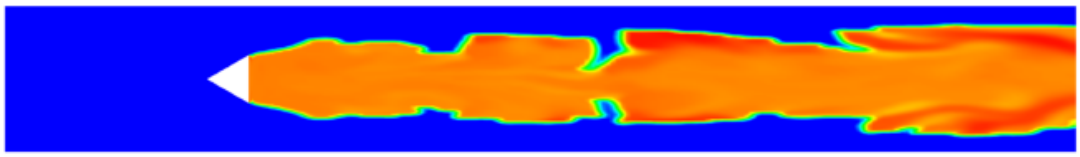

(b) Temperature contours of LEM sub-grid model 0.25 seconds after initialization with an equivalence ratio of 0.65.

Figure 4.3: Comparison of temperature contours of laminar combustion to LEM sub-grid model 0.25 seconds after initialization with an equivalence ratio of 0.65.

The time averaged normalized velocity profiles (Figures 4.9 and 4.10) show that the LEM-LES and laminar combustion predict similar velocity profiles at both locations. The LEM-LES velocity profile 0.015m downstream of the flameholder (Figures 4.9) does not match the experimental data along the centerline as well as the laminar reactive flow model, however, both models closely match the experimental data in the regions away from the centerline. Figure 4.10 shows that 0.15m downstream of the flameholder both models are again very similar and over-predict the centerline velocity. This higher centerline velocity prediction occurs for both models in accordance with the downstream measured locations, as shown in Figure 4.11. It can be seen, as in the temperature profiles, that the LEM-LES solver overall predicts values closer to the experimental data than does the laminar reactive flow model.

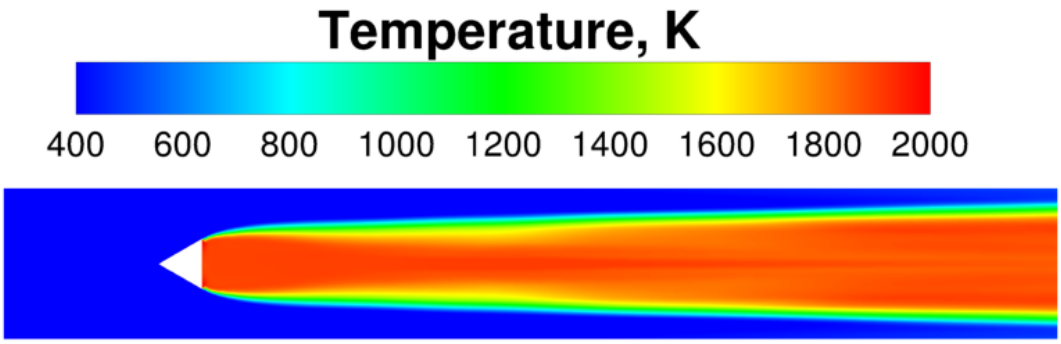

(a) Time averaged temperature contour of laminar closure model with an equivalence ratio of 0.65.

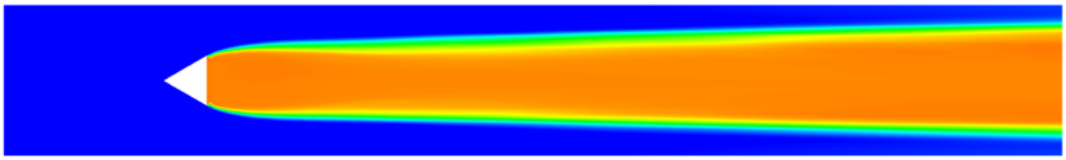

(b) Time averaged temperature contour of LEM sub-grid model with an equivalence ratio of 0.65.

Figure 4.4: Comparison of time averaged temperature contours of laminar reactive flow (a) to LEM sub-grid model (b) with an equivalence ratio of 0.65.

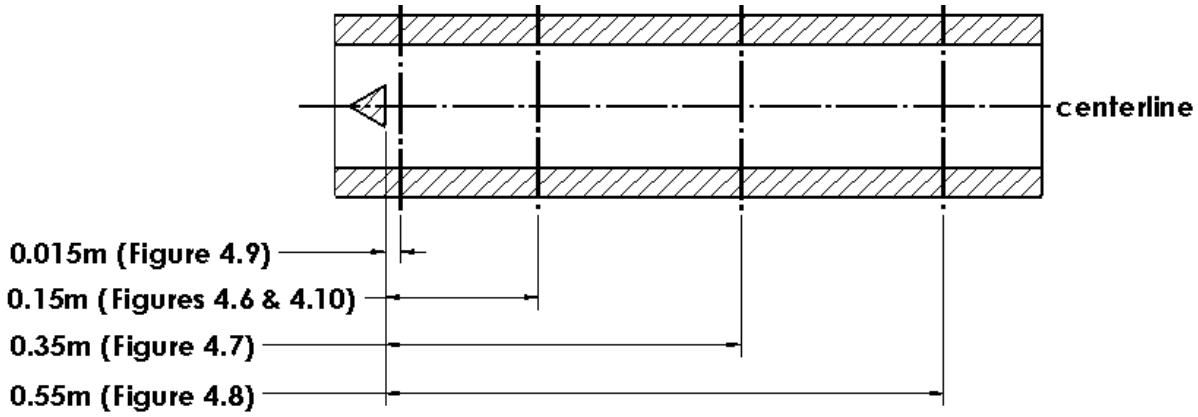

Figure 4.5: Locations downstream of the flameholder where the time averaged temperature and velocity profiles are measured.

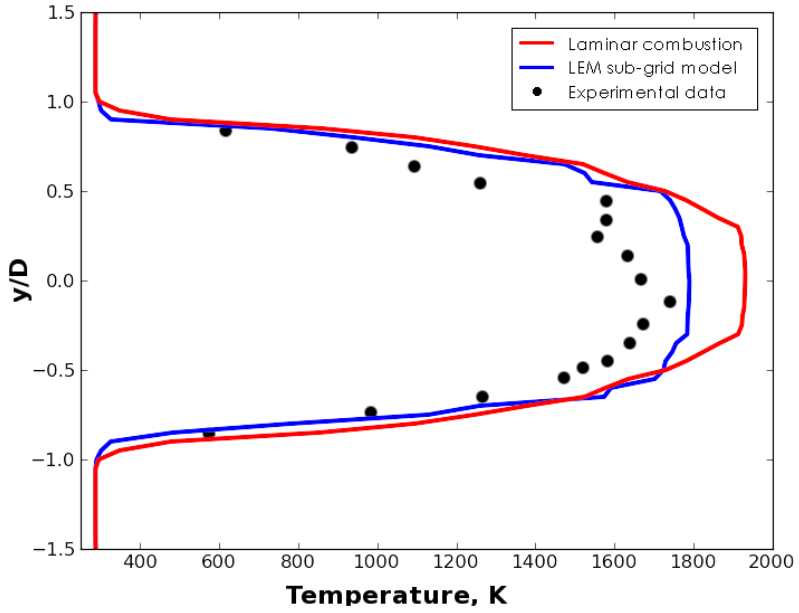

Figure 4.6: Temperature profile 0.15m downstream of flameholder for laminar combustion (red line) and LEM sub-grid (blue line) model compared to experimental data (black dots).

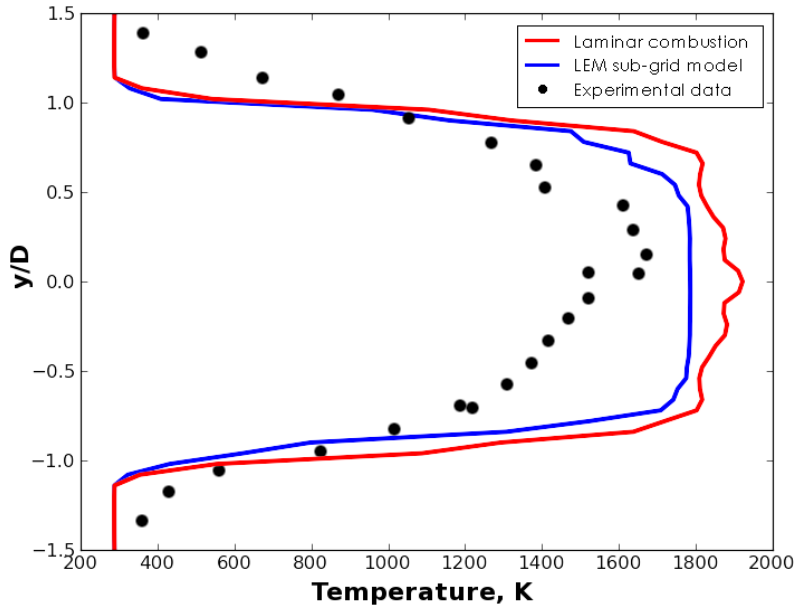

Figure 4.7: Temperature profile 0.35m downstream of flameholder for laminar combustion (red line) and LEM sub-grid (blue line) model compared to experimental data (black dots).

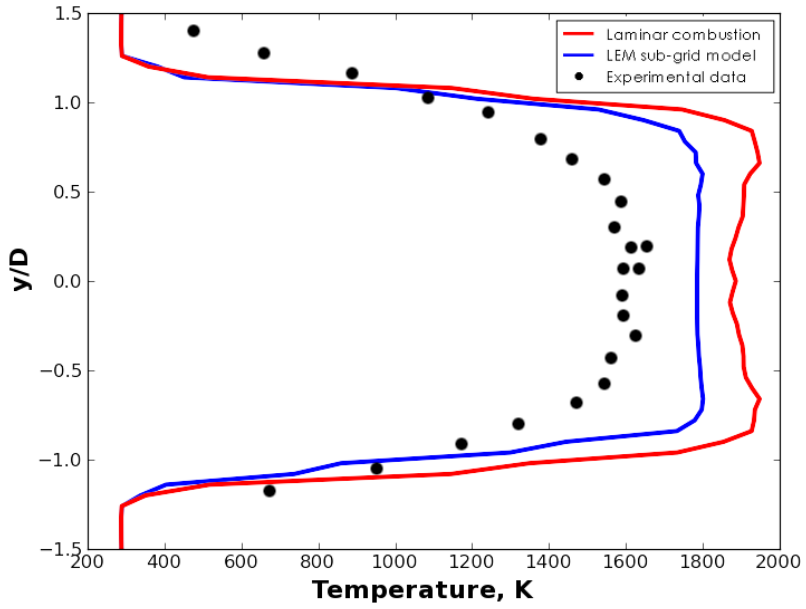

Figure 4.8: Temperature profile 0.55m downstream of flameholder for laminar combustion (red line) and LEM sub-grid (blue line) model compared to experimental data (black dots).

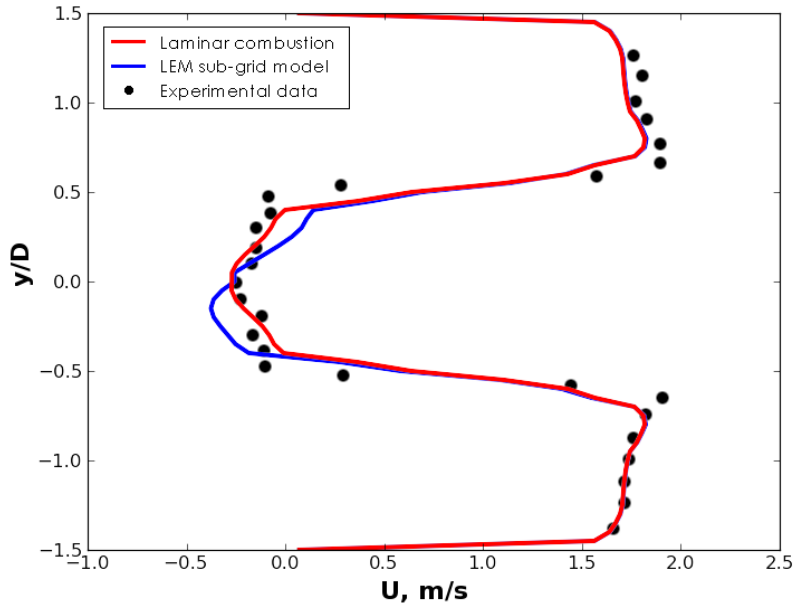

Figure 4.9: Normalized axial velocity profile 0.015m downstream of flameholder for laminar combustion (red line) and LEM sub-grid (blue line) model compared to experimental data (black dots).

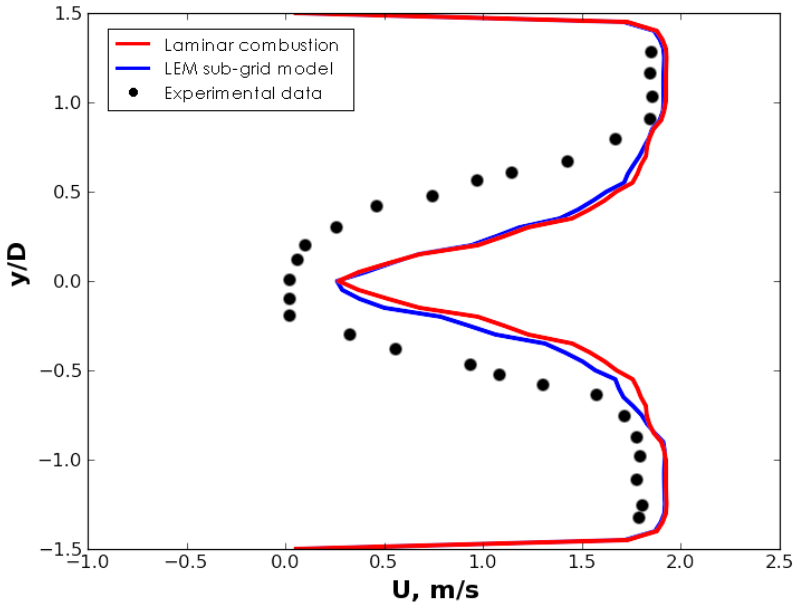

Figure 4.10: Normalized axial velocity profile 0.15m downstream of flameholder for laminar combustion (red line) and LEM sub-grid (blue line) model compared to experimental data (black dots).

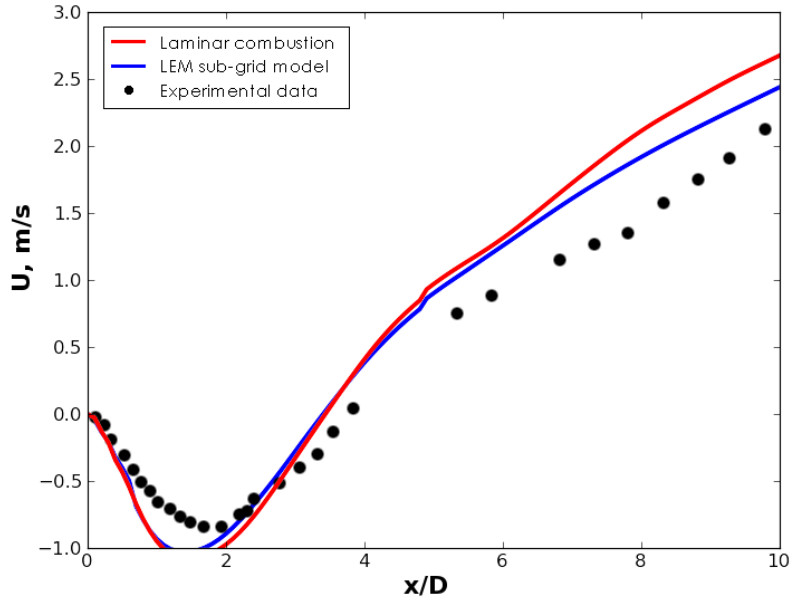

Figure 4.11: Centerline axial velocity of laminar combustion (red line) and LEM sub-grid (blue line) model compared to experimental data (black dots).

The LEM model is a multi-scale approach that solves an energy equation at both the resolved and sub-grid scales that results in two separate temperatures as discussed in Section 2.6. It is important to verify that the difference between these two temperatures is sufficiently small because an assumption of LEM is that the temperature can be discarded at the end of each physical time step. The magnitude of the difference between the LEM sub-grid temperature and the LES resolved temperature is calculated for the same flow parameters described in Section 4.2 and is shown in Figure 4.12. The results show that there is only a difference in temperature on the edges of the flame and the maximum is 4K.

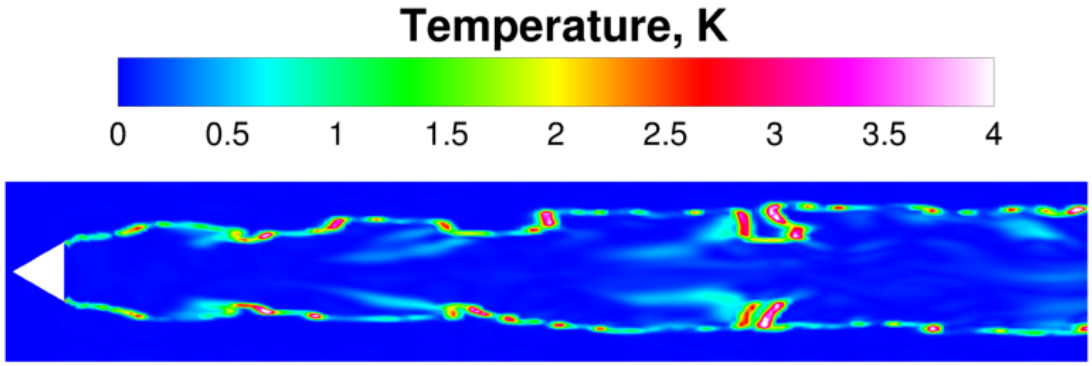

Figure 4.12: Magnitude of temperature difference between the resolved (LES) and sub-grid (LEM) temperature values.

4.3.2 Lean Blow-out

In order to test if the LEM-LES solver will properly predict lean blow-out the simulation was run on the same mesh as before but with an equivalence ratio of 0.50. Experiments have shown that the flame will blow-out at an equivalence ratio of 0.55 so the chosen equivalence ratio should produce blow-out. The simulation was initialized by running an equivalence ratio 0.65 for three flow through times to stabilize the flame. The inflow condition is then changed to an equivalence ratio of 0.50 and the simulation is continued. Figure 4.13a shows the instantaneous temperature contour of the stabilized combustion after the first three flow through times with an equivalence ratio of 0.65. Figure 4.13b shows the instantaneous temperature contours five flow through times after the equivalence ratio has been lowered to 0.50. It can be seen from these results that the flame temperature has significantly decreased with a reduction in equivalence ratio, as would be consistent with leaner combustion, but it does not achieve lean blow-out. The temperature directly

behind the flame holder has decreased from 1780 K to 1525 K and has re-stabilized at the lower temperature as seen in Figure 4.14.

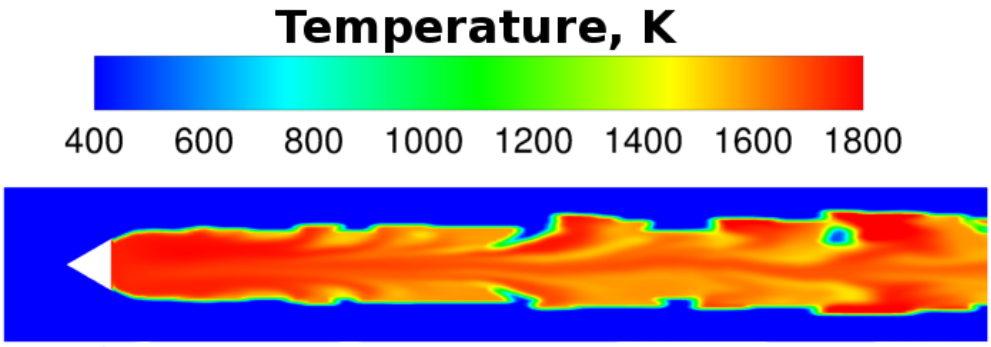

(a) Instantaneous temperature contour using the LEM-LES solver 0.26 seconds after initialization with an equivalence ratio of 0.65.

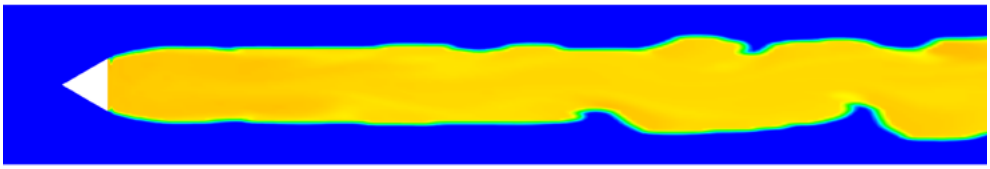

(b) Instantaneous temperature contour using the LEM-LES solver 0.412 seconds after changing the equivalence ratio from 0.65 to 0.50.

Figure 4.13: LEM-LES solver applied to the Volvo rig to predict lean blow-out.

4.4 Discussion

The LEM model is applied to the Volvo experimental rig to assess its viability as a sub-grid model for an LES solver. The results show that LEM-LES solver reasonably matches the experimental temperature downstream of the flameholder with an equivalence ratio of 0.65. The LEM-LES temperature is closer to the experimental data than a comparable laminar combustion model. LEM over-predicts the centerline velocity but again comes closer to the experimental data than the laminar solution. The addition of diffusion and advection of the LEM model have a noticeable effect on the solution. The difference in LES and LEM temperature is determined to be no greater than 4 K at any point in the simulation. This result means that there is no significant inconsistency in the resolved scale and sub-grid representation of the energy equation.

The LEM-LES solver does not properly predict lean blow-out at the experimentally-determined

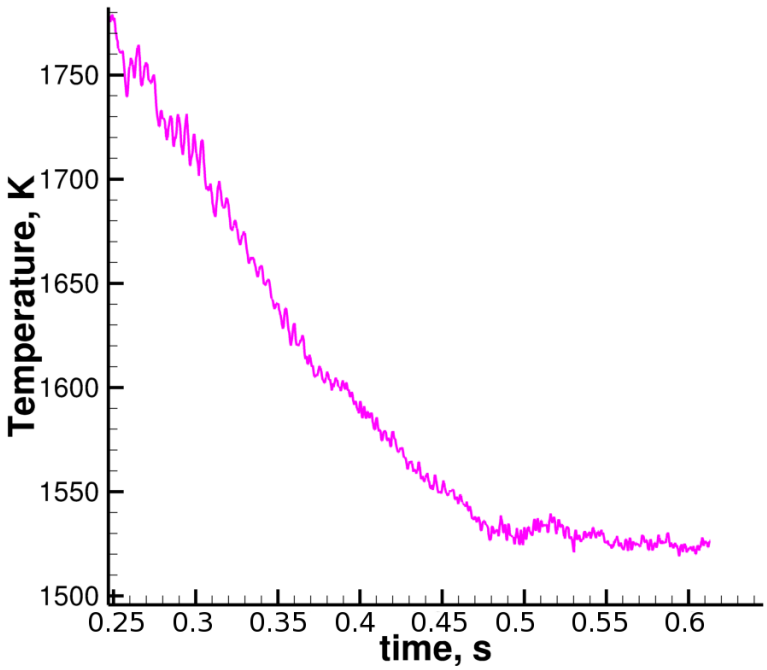

Figure 4.14: Temperature-time history after the equivalence ratio has been changed from 0.65 to 0.50 at a point 2.5 cm downstream of flameholder and 1.5 cm off the center line.

equivalence ratio. The flame has been shown in experiments to blow-out at an equivalence ratio of 0.55. In this work the LEM-LES solver does not capture blow-out even with a lower equivalence ratio of 0.50. The results show that the flame temperature behind the flameholder has decreased by 255K but has reached a relatively constant temperature, continuing to sustain combustion. The flame however is starting to show signs of blowing out in the region far downstream of the flameholder. This can be seen in the Kármán vortex shedding type profile of temperature that is present in this region (Figure 4.13b). It had been expected that the LEM model would predict lean blow-out at an equivalence ratio closer to the experimental data because the flame temperature is lower for a given equivalence ratio than with the comparable laminar combustion closure model.

A possible reason for the discrepancy is with the initialization of the LEM profiles at the beginning of each sub-grid calculation (ref Section 2.4.2). At each LES time step the LEM solution is re-initialized to a linear profile. This means that the turbulence from earlier sub-grid calculations (i.e. previous LES time step) is neglected. The model only performs stirring for a small number of times during each sub-grid calculation which could mean that the model does not produce the

appropriate degree of turbulence. The lack of proper representation of turbulence is one possible reason for the improper prediction of lean blow-out.

Additionally, the reaction mechanism used in this simulation is a single step propane reaction. This is a significant simplification when compared to a physical flame that contains hundreds of associated reactions in conjunction with the global reaction. This current approach does not represent processes such as the formation of hydrogen radicals that are generally involved with ignition and extinction and can cause the lean blow-out prediction to be erroneous.

CHAPTER 5

Effects of Boundary Treatment on Thermo-acoustic Predictions

Numerical simulations are is an invaluable tool for engineers because they can be used to optimize and eliminate design configurations before test articles are built. Simulations can also provide insight and diagnostics for regions which are difficult to experimentally interrogate. However, CFD calculations can take months of computational time to produce a solution for complex unsteady configurations. For bluff-body stabilized flames, a common simplification used to reduce computational time is to eliminate the farfield portion of the plenum or exhaust section behind the combustor. The risk in reducing the size of the domain is that the artificial boundary conditions that are imposed may not be physically representative of the actual experiment, and as the boundary moves closer to the region of interest it may alter the solution. This chapter focuses on the effect of the outlet boundary condition on the thermo-acoustic response inside a combustor. The experiment chosen for this study is a bluff body rig used at the AFRL. CFD is used to examine the effect of multiple outlet boundary conditions in an effort to produce an optimum design for the experiment while simultaneously showing the effect that the outlet boundary condition can have on the modeled flow inside the combustor.

5.1 Description of the Bluff-Body Configuration

The rig used in this study was designed by AFRL at Wright-Patterson Air Force Base to study bluff body stabilized turbulent flames to better understand the behavior of augmentors in gas turbine engines. The test section is a 12.7 cm (5 in) by 15.24 cm (6 in) rectangular duct with a 3.81 cm (1.5 in) bluff body equilateral triangle spanning the 15.24 cm width. Premixed fuel and air is injected through a perforated plate upstream of the test section with flow rates ranging from 0.181 kg/s (0.4

lbm/s) to 0.318 kg/s (0.7 lbm/s). The flow exits the duct and travels into a 34.70 cm (13.66 in) circular exhaust tube 60.96 cm (24 in) downstream of the duct exit. Figure 5.1 shows the schematic of the rig.

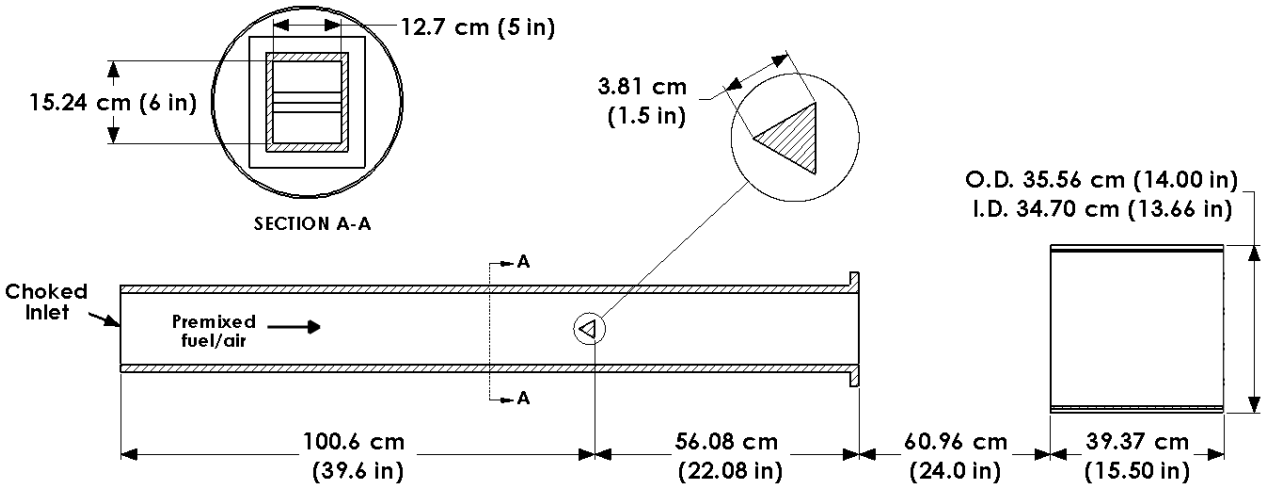

Figure 5.1: Cross-sectional view of the bluff-body combustor rig geometry.

Within practical flow regimes, the triangular flameholder in the rig creates a recirculation zone directly downstream of its trailing edge, trapping hot products and serving as a source of heat to ignite the incoming fuel and oxygen mixture. A shear layer forms downstream from the flameholder between the main flow and recirculation region, allowing for improved mixing between the hot and cold gases. Figure 5.2 shows the typical re-circulation region created by the flameholder for the flow conditions studied here.

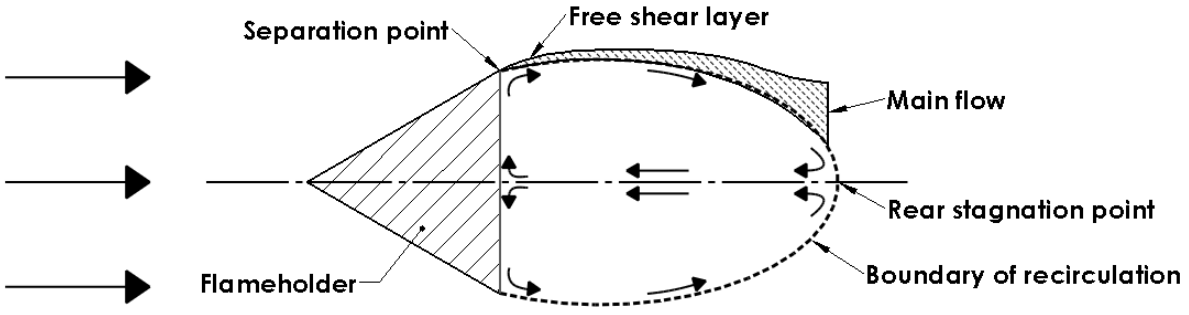

Figure 5.2: Recirculation behind a triangular bluff body (Adapted from [45]).

5.2 Preliminary Design Study

A concern for the experimental rig designers was that air from the downstream farfield would get drawn into the test section and influence the flowfield. The addition of a nozzle to the downstream end of the rig was proposed to minimize this effect. The higher speed exhaust would prevent any mass from the surroundings from being drawn into the test section. The idea was explored by running a computational study that added a nozzle to the duct exit. The streamlines and the pressure contours were examined to see how the outside air interacted with the exhaust air from the duct exit. The study was performed with three configurations; a baseline configuration with no nozzle, a 5° nozzle, and a 10° nozzle at the duct exit. These configurations are shown in Figure 5.3. The CFD simulations were conducted in GEMS using a two-dimensional non-reacting fluid flow to study the effect of the nozzle. The flow was driven by injecting hot air at 2200 K into the duct. The farfield was initialized with atmospheric conditions, air at a pressure of 101 kPa and a temperature of 288 K. The simulations were run for three flow-through times so that the results could be analyzed after the initial transients had dissipated.

A comparison of the vorticity contours resulting from these configurations shows that all three cases exhibit Kármán vortex shedding off of the flameholder, as seen in the right side of Figure 5.4. The presence of the nozzle does not appear to affect this phenomenon in any appreciable way. The pressure in the duct, however, is sensitive to the presence of the nozzle, as indicated in the left side of Figure 5.4. It can be seen that as the nozzle angle increases, so does the bulk pressure in the duct. This can easily be seen in Figure 5.4c where the scale is adjusted to capture the pressure variation in the vortex shedding. In this configuration the maximum pressure is 104 kPa which is larger than in Figures 5.4a and 5.4b where the maximum pressure is 102 kPa.

The streamlines are superimposed on the axial velocity contours to visualize the flow, as seen in Figure 5.5. It is clear from the streamlines that none of the exterior flow in the baseline configuration (Figure 5.5a) is drawn into the duct. The nozzle configuration results show that the velocity is increased downstream of exit and even more exterior flow is being drawn into the exhaust due to entrainment. Hence, in both nozzle configurations (Figure 5.5b and 5.5c) as well as the baseline, the streamlines indicate that there is no appreciable flow from the farfield being drawn upstream into the duct.

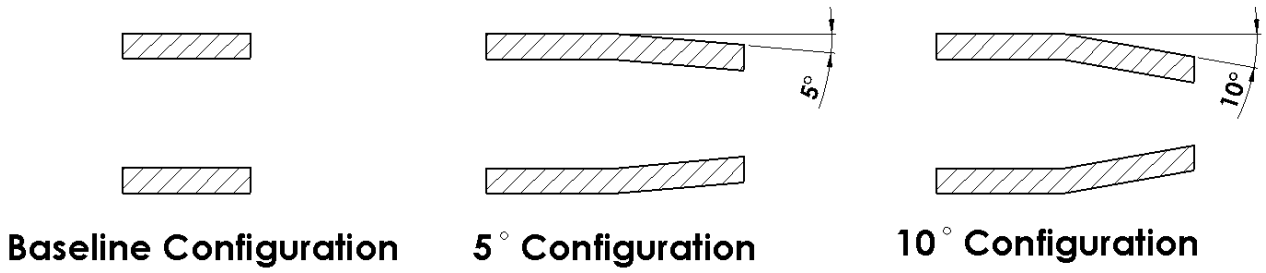

Figure 5.3: The duct exit of the three configurations in this study. The baseline configuration does not have a nozzle at the exit (left). The nozzle configurations have a 5° (middle) and 10° (right) nozzle at the duct exit.

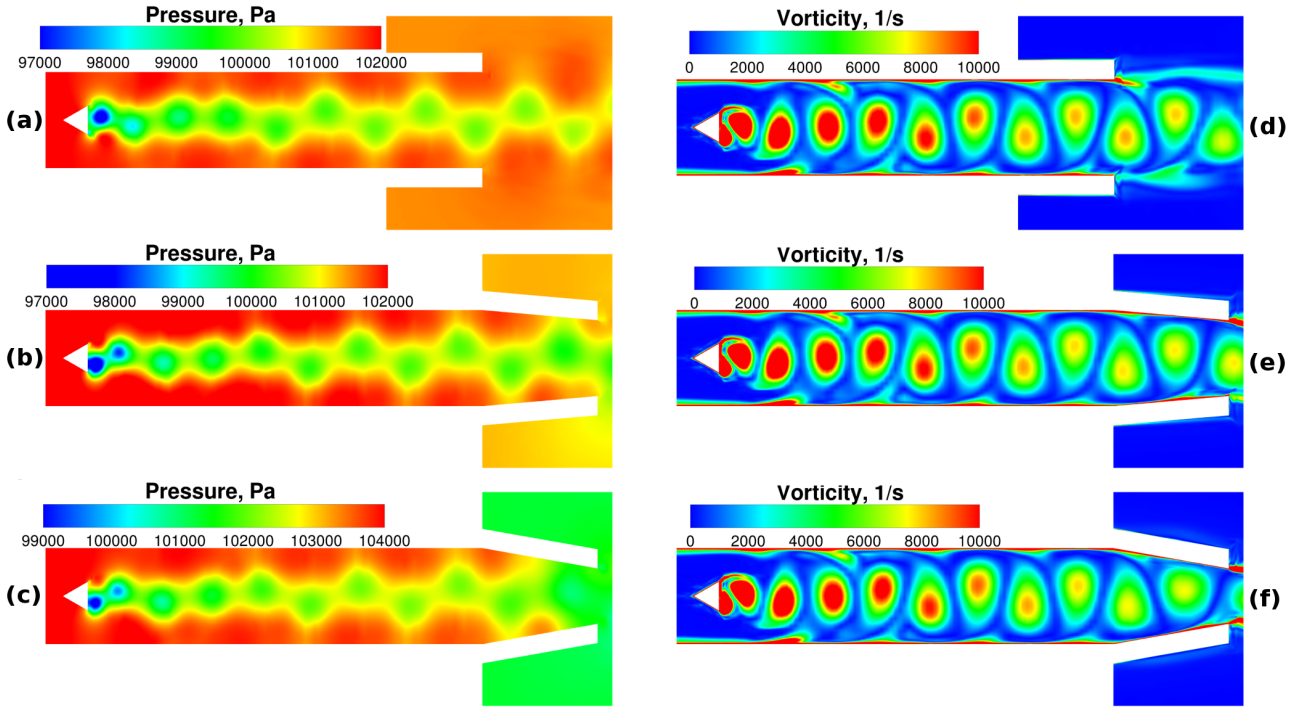

Figure 5.4: Contour plots of the static pressure (left) and vorticity (right) are plotted for the three computational domains analyzed. The baseline configuration, 5° nozzle, and 10° nozzle are shown on the top, middle, and bottom, respectively.

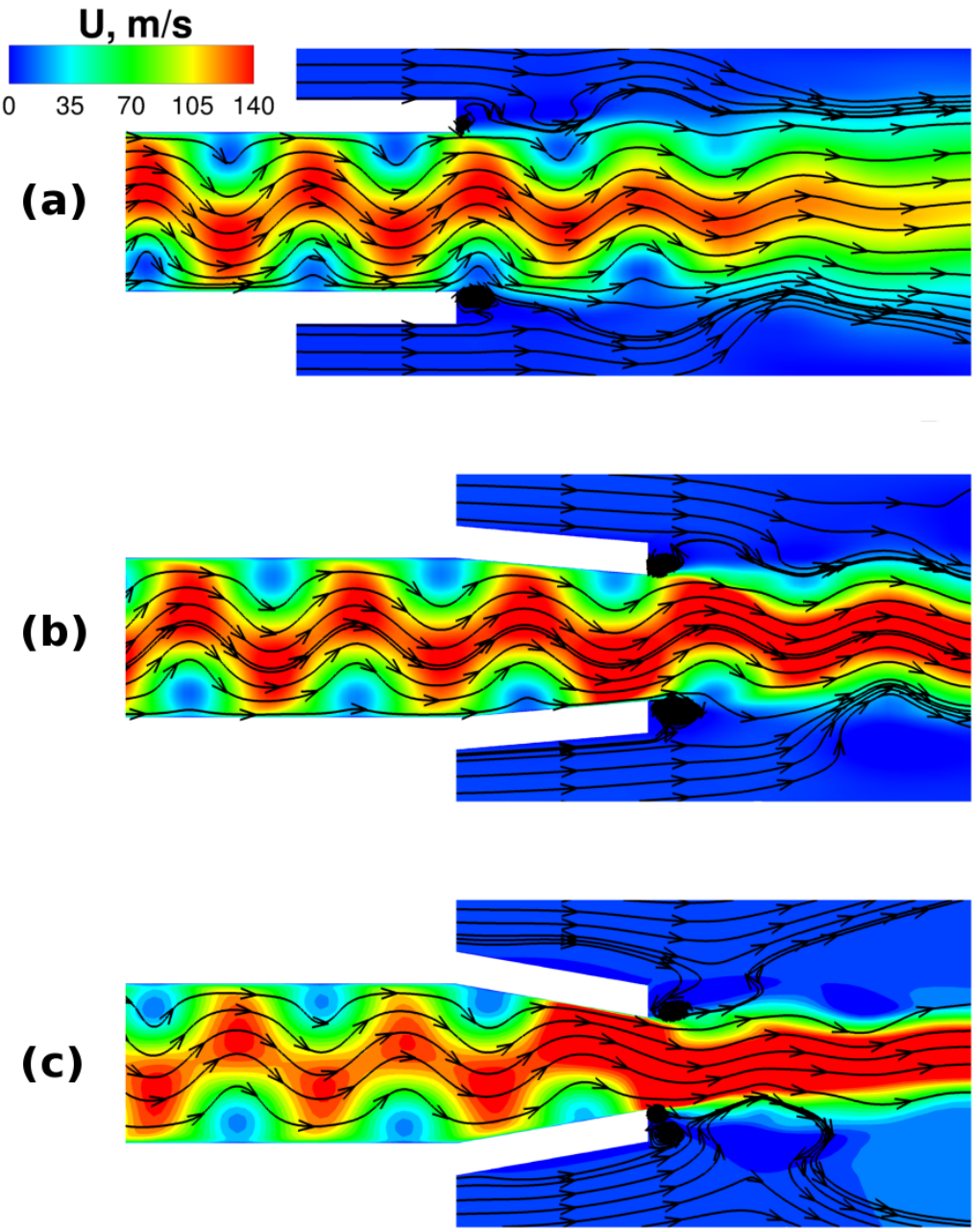

Figure 5.5: Contour plots of axial velocity with super-imposed streamlines are plotted for the three computational domains analyzed. The baseline configuration, 5° nozzle, and 10° nozzle are shown on the top, middle, and bottom, respectively.

5.3 Computational Grids and Boundary Conditions

Four different exit boundary types are considered in this study. Figure 5.6 shows each of the geometries. The four configurations implemented in this section are: imposed back pressure, exhaust plenum, and two experimental configurations. Experimental configuration one represents an early experimental geometry of the rig while experimental configuration two matches the current experimental configuration, as seen in Figure 5.1. The imposed back pressure grid contains 31,050 cells and is the least computationally expensive of the four meshes. This configuration models only the duct and does not include the exhaust section. The boundary conditions are mass inflow at the duct inlet, no slip for the walls and flameholder, and outflow at the exit with an imposed atmospheric pressure of 101 kPa.

The exhaust plenum configuration contains 58,342 cells. The height of the plenum is twice the length of the duct and the length is four times the duct length. All plenum boundaries use an inflow/outflow boundary condition that allows flow to either enter or exit the domain depending on the local conditions. A pressure gradient is imposed across the length of the plenum in order to reduce the possibility of inflow through the exit plane. The pressure on the left is 105.5 kPa while the pressure on the right is 101 kPa. The cells in the farfield get larger away from the duct exit in order to minimize wave reflection off the artificial boundary surface. This configuration is the most physically desirable domain because it represents the flow exhausting into a large plenum section, avoiding any potential for downstream influences.

The first experimental configuration contains 50,828 cells. The farfield has a 17.78 cm region of inflow/outflow with a pressure of 105.5 kPa immediately downstream of the duct exit followed by a 106.68 cm slip wall. The wall is modeling the exhaust duct that collects the flow downstream of the experiment. The flow is exhaust from the domain through an inflow/outflow boundary with a pressure of 101 kPa. The pressure gradient is added to reduce numerical instabilities by constantly exhausting the flow downstream.

The second experimental configuration contains 46,319 cells. This setup has the same boundary conditions as the first experimental configuration with the exception of moving the exhaust duct in the farfield to be 60.96 cm downstream of the duct exit. The wall length is also shortened to be 39.37 cm.

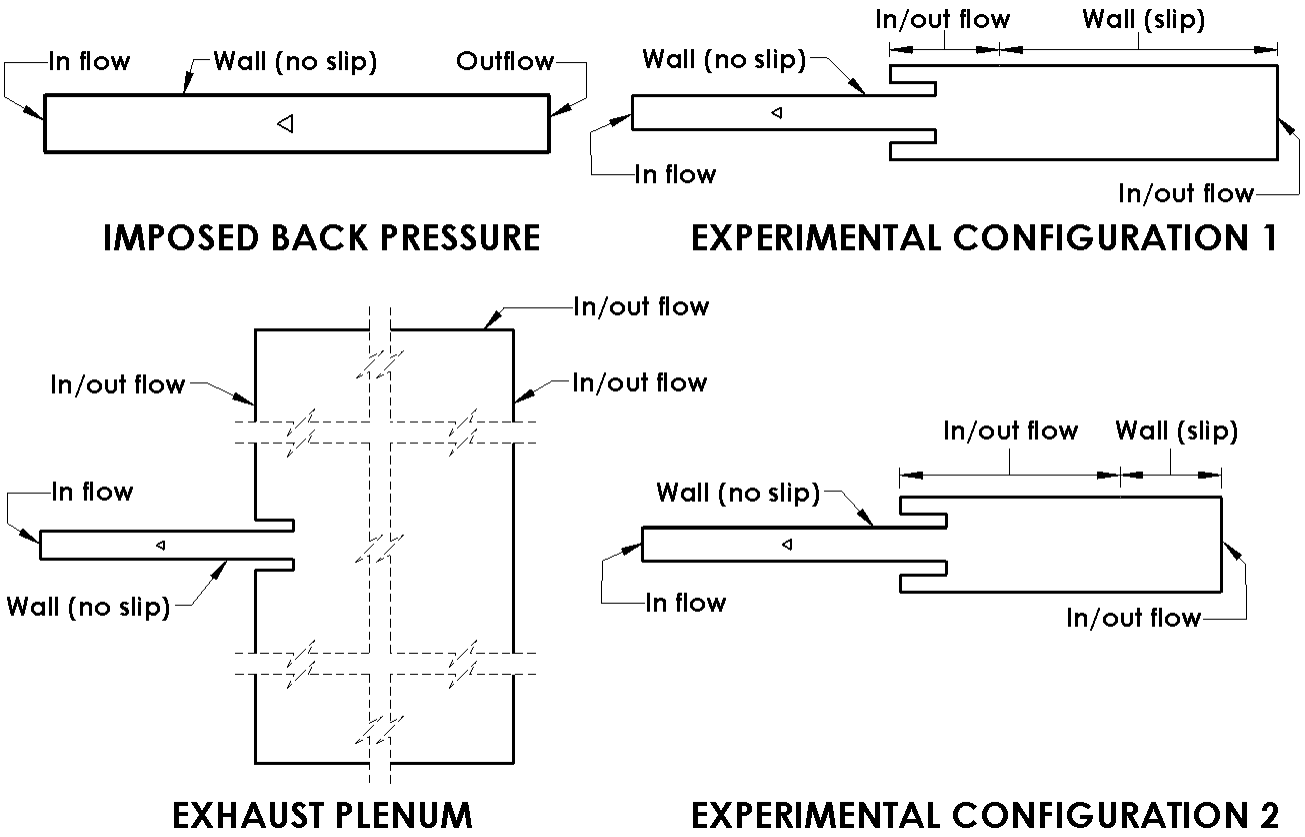

Figure 5.6: Exhaust boundary conditions and computational geometries.

5.4 Effect of the exit boundary condition for non-reacting flow

The effect that boundary conditions and domain geometry have on a non-reacting flow field was tested on the rig. Simulations were run using the imposed back pressure, the exhaust plenum, and the first experimental configuration in order to compare how different outlet boundary conditions affect the results. The simulations were two-dimensional non-reacting flow and were carried out using GEMS. The flow was driven by injecting hot air at 2200 K into the duct. The farfield was initialized with atmospheric conditions, air at a pressure of 101 kPa and a temperature of 288 K. The simulations were run for three flow-through times so that the results could be analyzed after the initial transients dissipated.

A comparison of the vorticity contours shows that all three cases exhibit Kármán vortex shedding off of the flameholder, as shown in Figure 5.7. The pressure contours also show excellent correspondence to vorticity for the three configurations, and few differences among the configura-

tions. It appears that, at least qualitatively, the presence of the exhaust duct or the imposition of the back pressure condition did not affect the flow features in a significant way for non-reacting flows.

To further compare the three domains the time history of the unsteady pressure was recorded at a location 0.38 cm downstream of the flameholder 1.78 cm off the center line. To examine the frequency content of the signal a power spectral density (PSD) analysis was performed. A total of 150 ms of temporal data were analyzed, with the data spaced 1 μs apart which resulted in a maximum frequency of 2000 kHz and a frequency resolution of 6.67 Hz. It can be seen from Figure 5.8 that the spectral content for all three configurations have strong, well defined peaks at 725 Hz, 1450 Hz, 2175 Hz, and 2900 Hz. The peaks in all three configurations have a similar amplitude. These frequencies correspond to the Kármán vortex shedding and its higher harmonics. The exhaust plenum and the experimental configuration also have well defined peaks at 600 Hz and 1300 Hz. These two frequencies correspond to the vortex shedding at the exit plane of the duct and are not found in the imposed back pressure case because the artificial boundary condition precludes vortex shedding from taking place. With the exception of the modes due to the vortex shedding at the exit plane the three configurations have similar behavior. For the non-reacting case, these results therefore indicate that: (1) the experimental configuration reasonably represents a large exhaust plenum, and (2) the imposition of the exit boundary condition is a reasonable computational model of the experiment. In the next section, we examine whether these conclusions hold for the reacting case wherein the dynamics is not caused by vortex shedding, but by thermo-acoustic coupling.

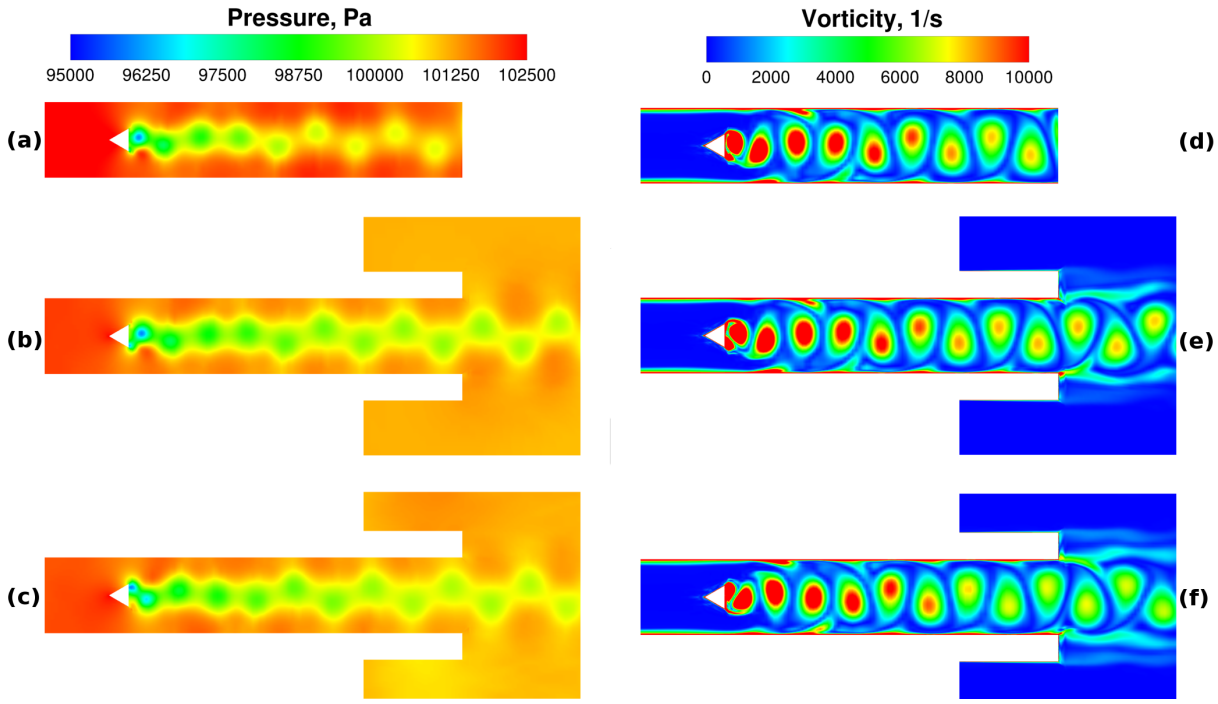

Figure 5.7: Contour plots of the static pressure (left) and vorticity (right) are plotted for the three computational domains analyzed. The imposed back pressure, exhaust plenum, and experimental configuration one are shown on the top, middle, and bottom, respectively.

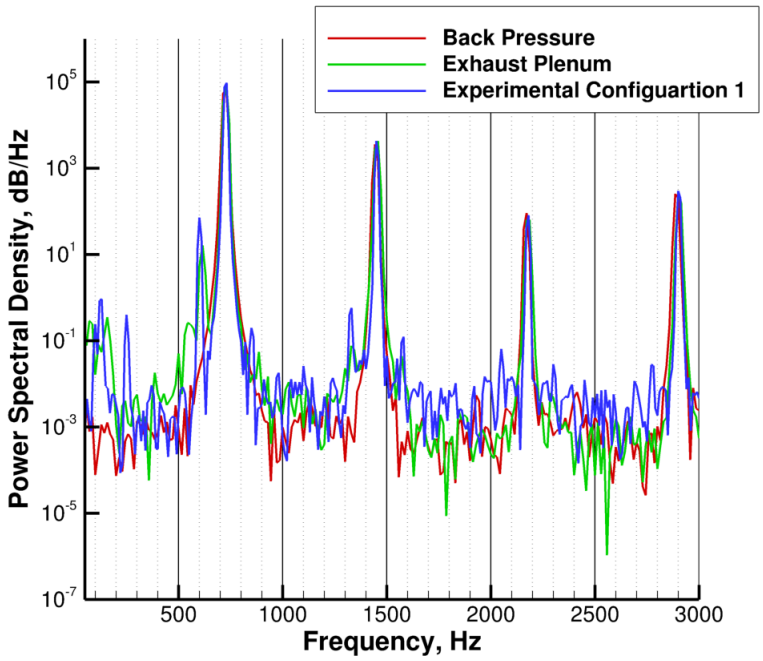

Figure 5.8: PSD of the static pressure in non-reacting flow at a point located 0.38 cm downstream of the flameholder and 1.78 cm off the center line.

5.5 Effect of the exit boundary condition for reacting flow

In premixed combustion behind a flameholder the combustion will usually suppress the von-Kármán vortex shedding. Therefore it is expected that the spectral content of the pressure signals may be very different for reacting flow compared with its non-reacting counterpart. The prior three domains that were considered for the non-reacting study are repeated here using a reacting flow setup. In addition, the second experimental configuration which has the exhaust duct wall moved further downstream was also tested. The purpose of this modified configuration was to further minimize any effects that the exhaust duct may have on the reacting flowfield within the main duct. Premixed propane and air were introduced into the domain with an equivalence ratio of unity and a temperature of 288 K. The mass flow was 0.297 kg/s. In order to ignite the flow the domain was initially filled with warm combustion products at a temperature of 1792 K. The simulations were run with the GEMS CFD solver using a single step global reaction [46]. The simulations were run for three flow-through times so that the results could be analyzed after the initial transients dissipated.

A comparison of the temperature contours shows that the four computational domains produce very different results, which can be seen in Figure 5.9. The imposed back pressure domain (Figure 5.9a) produces a more uniform temperature profile downstream of the flameholder perhaps because the artificial boundary condition enforces a constant pressure at the duct exit. The exhaust plenum domain (Figure 5.9b) removes the constant pressure restriction at the exit which is the ideal situation since it allows the combustor to experience farfield pressure effects. This result shows the presence of pressure oscillations and a pulse-like appearance in the temperature contours. The original experimental configuration (Figure 5.9c) is greatly affected by the pressure reflections off of the exhaust duct wall in the farfield. In this configuration the wall is located 17.78 cm downstream of the exit and the oscillatory pressure reflections cause the hot gas to travel upstream at certain times in the cycle. In the modified experimental configuration (Figure 5.9d) the exhaust duct wall is moved further downstream which causes the flow to be less affected by the pressure reflections than in the original experimental configuration, however, it still shows some differences compared to the exhaust plenum case.

It is clear in the reacting flow cases that the farfield boundary conditions greatly affect the flow features in the duct. To get a qualitative idea of this the pressure time-histories were taken

at the same point as in section 5.4, directly behind the flameholder, and are shown in Figure 5.10. The results again show that there is a significant difference among the four domains. A noticeable difference between the plots is the amplitude of the oscillations. In the first experimental configuration (Figure 5.10c) the pressure oscillates about 20% from the mean values compared to 5% for the imposed back pressure (Figure 5.10a) and 10% for the exhaust plenum and the second experimental configuration (Figures 5.10b and 5.10d). In fact, these results confirm that the second experimental configuration indeed represents the ideal plenum geometry reasonably well.

The PSD analysis of the pressure time history is shown in Figures 5.11 and 5.12. A total of 200 ms of temporal data was analyzed. The data were spaced 0.5 μs apart which resulted in a maximum frequency of 4000 kHz and a frequency resolution of 5.0 Hz. It can be seen that all four configurations have peaks at the same frequencies but with different amplitudes. The von-Kármán vortex shedding that dominated the non-reacting case is suppressed in the reacting case, as expected, and the acoustic pressure modes are dominant. From Figure 5.11 it can be seen that the imposed back pressure case has the lowest amplitude which directly corresponds to the smallest oscillation from the mean seen in the time-history. The exhaust plenum and the second experimental configuration PSDs agree very well despite having somewhat different temperature profiles. The first experimental configuration has the highest magnitude due to the large pressure oscillations seen in the time-history plots. Additionally, Figure 5.12 shows the imposed back pressure case has a high PSD amplitude at 3200 Hz. This amplitude appears to be a computational artifact that occurs because of the artificial boundary condition imposed on the domain and is not evident in any of the other three cases that involve the exhaust plenum section.

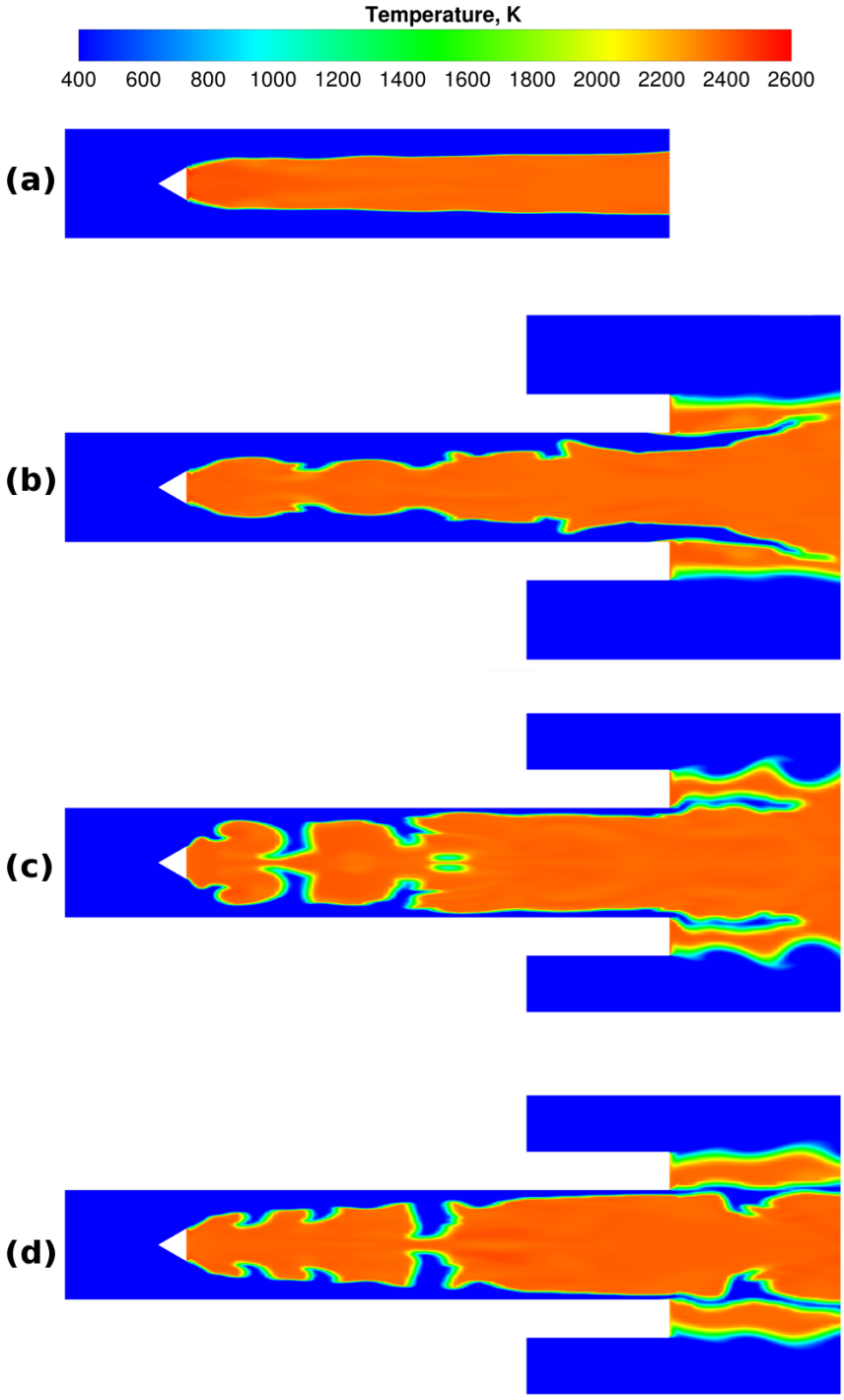

Figure 5.9: Contour plots of the temperature are plotted for the four computational domains analyzed. The imposed back pressure, exhaust plenum, experimental configuration one, and experimental configuration two are shown from top to bottom.

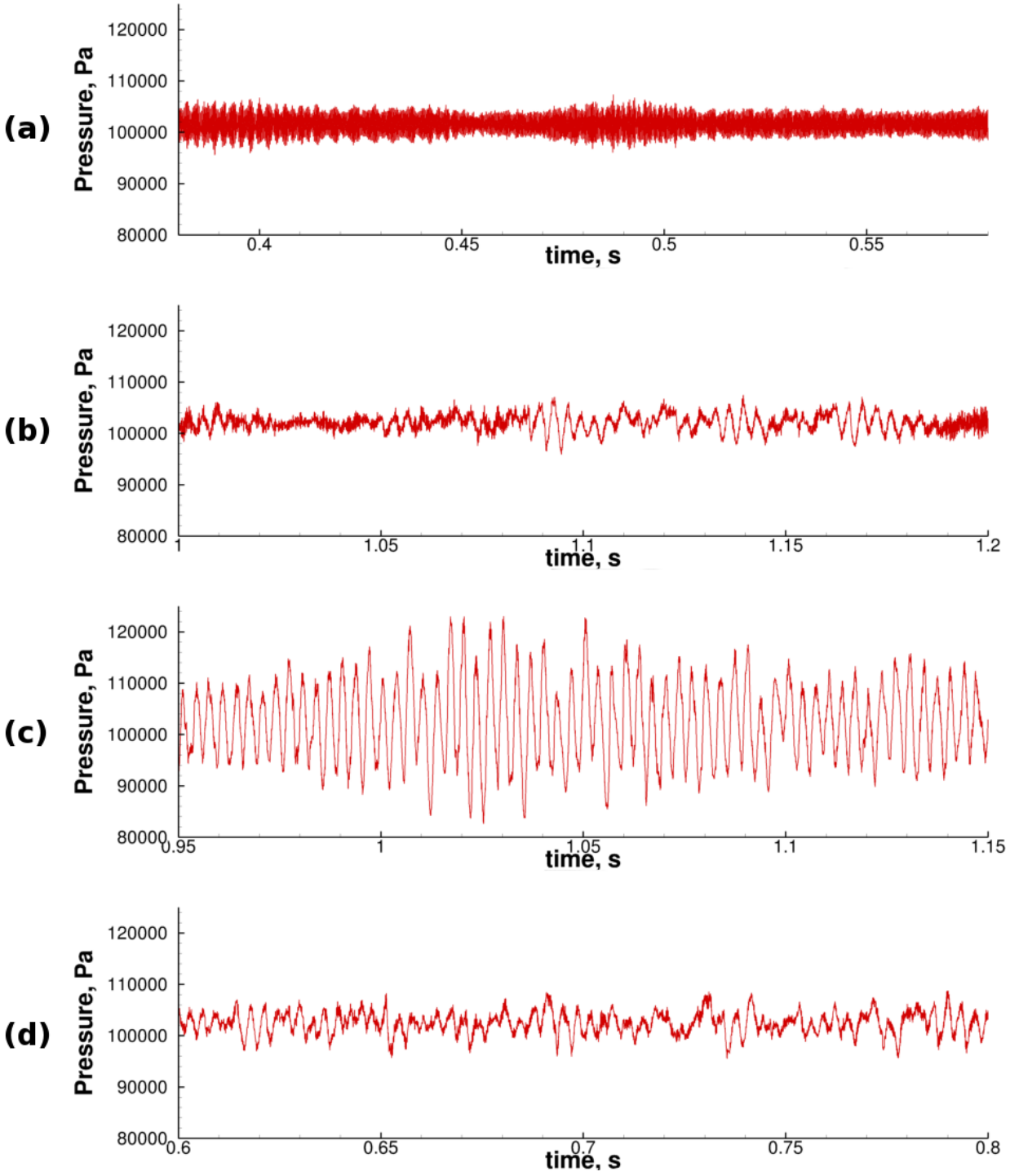

Figure 5.10: The pressure-time history is plotted for the four computational domains analyzed. The imposed back pressure, exhaust plenum, experimental configuration one, and experimental configuration two are shown from top to bottom.

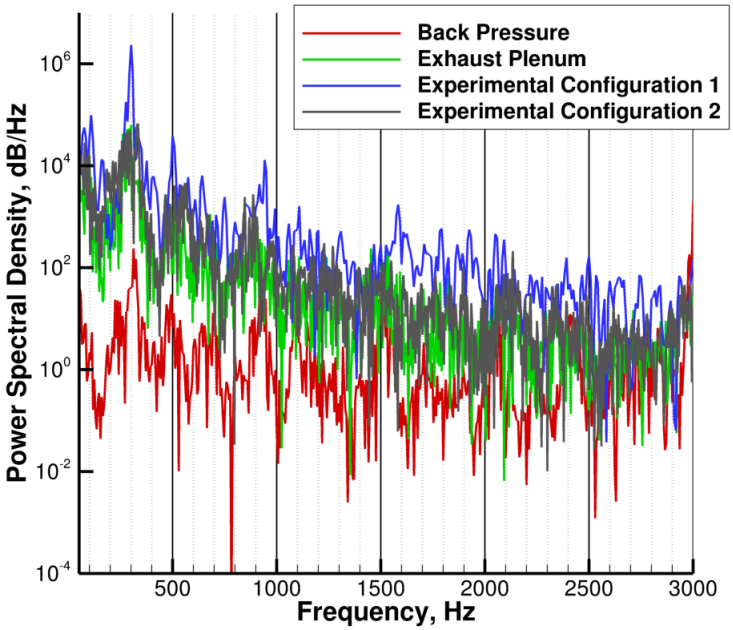

Figure 5.11: PSD of the static pressure in reacting flow at a point located 0.38 cm downstream of the flameholder and 1.78 cm off the center line. (0-3000 Hz).

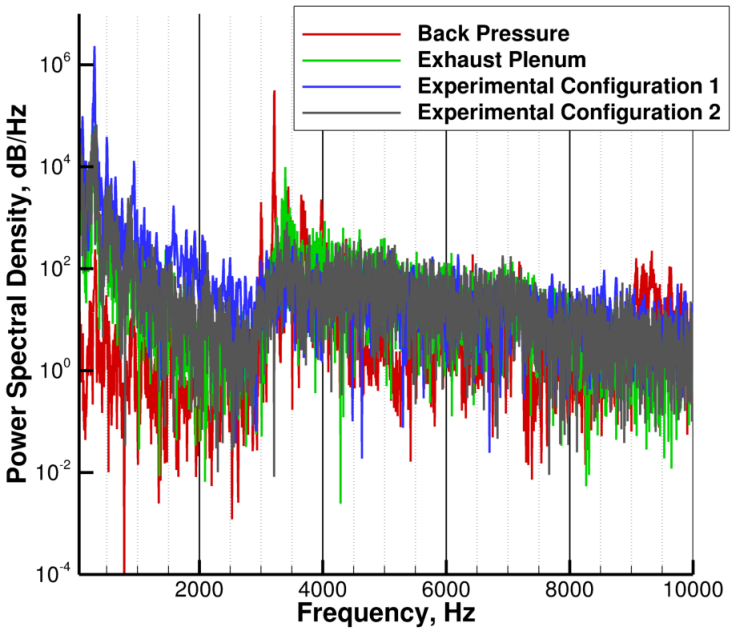

Figure 5.12: PSD of the static pressure in reacting flow at a point located 0.38 cm downstream of the flameholder and 1.78 cm off the center line. (0-10000 Hz).

5.6 Conclusions

The type of exit boundary condition was examined using both non-reacting and reacting flows in order to better understand the influence of the boundary condition on the spectral content of the pressure waves inside the combustor. The study was also used to help design the experimental rig by evaluating the facility effects. In particular a nozzle was added in an effort to eliminate reverse flow into the combustor from the ambient. This design change was determined to be unnecessary because the baseline configuration without the nozzle showed little or no reverse flow into the combustor from the facility.

The non-reacting flow study compared the vorticity and PSD for the ideal computational (imposed back pressure), ideal physical (exhaust plenum), and experimental configurations. All three cases produced similar results with the only difference being the shedding off of the nozzle exit in the latter two cases which does not seem to materially affect the flow in the reacting duct.

The four reacting results were very different from the non-reacting results. The temperature profile, pressure time-history, and PSD analysis are heavily dependent on the outlet boundary condition. The presence of the exhaust plenum (the ideal instance) shows that the temperature contour and pressure oscillations are strongly affected by the external flow. Adding the exhaust duct wall as in the experimental configuration creates pressure reflections which further affects the solution in the combustor, however, it is less dramatic when the wall is moved further downstream. Indeed, the exhaust plenum and the second experimental configuration had similar pressure oscillation magnitudes and similar PSD profiles despite having different temperature profiles. It is worth noting that all four configurations showed excitation at the same frequencies but had different amplitudes which suggests that the plenum region influences the thermo-acoustic oscillations in the duct. It can therefore be determined that it is necessary include the proper outlet condition when modeling experiments because the artificial boundary condition (imposed back pressure) does not capture the correct pressure effects and also shows what appears to be non-physical high frequency content. This study shows that boundary conditions and facility configuration can affect the computational solution and are important to consider when performing detailed simulations.

CHAPTER 6

Conclusion and Future Work

6.1 Summary

This work analyzed the three main aspects of bluff-body stabilized flames: stationary combustion, lean blow-out, and thermo-acoustic instabilities. Stationary combustion and lean blow-out prediction were studied using an improved version of the LEM sub-grid model coupled with the GEMS solver. The LEM model in this work is used to close the filtered species production term in the large scale species mass fraction equations. In previous work the LEM model accounted for the species mass fraction within the domain solely in the sub-grid, where as in this version the species equations are solved at the resolved scale. The advantage of this method is that advection and diffusion between LES cells is correctly represented. The results showed that LEM-LES over predicts both the temperature and velocity profiles downstream of the flameholder, however, the simulation does better than a comparable laminar closure model in capturing the temperature field. The LEM-LES solver did not predict lean blow-out at the proper equivalence ratio. Experiments have shown a premixed propane flow in the Volvo rig to blow out at an equivalence ratio of 0.55 and in this work an equivalence ratio of 0.50 with the LEM-LES solver did not produce blow-out. Therefore, it can be concluded that the present implementation of LEM-LES solver provides some improvement for reactive flow predictions of velocity and temperature, however, the model is not sufficient to predict flame extinction correctly. More work is needed to improve the LEM model in order to better predict the complex dynamics involved in turbulent combustion including the exploration of more sophisticated chemical kinetics mechanisms than the global chemistry used in this study.

The thermo-acoustic instability analysis demonstrates that boundary condition effects are important to considered when performing both non-reacting and reacting simulations. In reacting flows especially, imposing a non-physical boundary condition at the duct exit suppresses the acous-

tic content inside the domain and alters the temperature contour downstream of the flameholder. The addition of a wall in the exhaust plenum creates pressure reflections that also effect the thermo-acoustics inside the duct and is necessary to consider when performing simulations. Therefore, it can be concluded that it is important to include proper farfield geometry when performing calculations so that non-physical boundary conditions do not influence the solution.

6.2 Advantages and Disadvantages of LEM-LES

The LEM model is attractive because it has validity for all flame regimes and it solves the full species equations on the sub-grid level of an LES grid. The model is able to capture species production and diffusion while providing an reasonably accurate representation of turbulence through the triplet mapping process. The equations are solved in one dimension making the solution much less computationally expensive than running a DNS and is therefore applicable to flows with higher Reynolds numbers.

The LEM model is computationally expensive because it solves an ODE at each LEM node within the sub-grid. In areas where there are large gradients there can be as many as thirty-six ODEs being solved for a single LEM line. It is estimated to be about five times slower than a comparable laminar closure model although this number is likely to be problem dependent. Additionally, the constant pressure assumption in the LEM model makes it applicable only in flows where compressibility effects are not important. This limits its effectiveness in many aerospace flows and acoustic analysis.

6.3 Future Research

Despite its advantages, the LEM model did not properly capture the experimental conditions for lean blow-out. One possible reason for this discrepancy could be in the linear initialization process of each LEM line. After the LEM solution has been advanced to the next physical time step the profile is discarded and initialized as a new linear profile during the next time step (Reference Section 2.4.2). This does not allow the stirring to produce a proper turbulent profile in the sub-grid. In future research the LEM profile can be retained after each time step so that the turbulence from previous time steps is retained in the sub-grid making the model more representative of a

physical flow. In doing so it will be important to make the total concentration of species within each LEM sub-grid line match the resolved species concentrations from the LES solver so that the model is physically representative.

The LEM implementation in this work treats each LEM line as a self contained entity in which there is no advection or diffusion between LEM lines occur. This approximation may also be contributing to the erroneous lean blow-out prediction seen in the Volvo rig geometry. It would therefore be important to further the model so that these physical phenomena are properly captured in the sub-grid. Additionally, future simulations should be run with a finer mesh downstream of the flameholder because the 4mm spacing may be too coarse to properly capture the small length scales involved in this problem. It would also be interesting to run the simulation in three dimensions so that the flow properties are better represented than in the two dimensional simulations presented in this work.

Finally, the reaction kinetics used in the Volvo rig simulations was a single step global propane reaction. This is a significant simplification because it does not account for the many possible associated reactions (perhaps in the hundreds) that occur in a physical flame. Future work should run the same simulation using a more complex mechanism that takes into account intermediate species such as radical species that are produced, many of which are associated with ignition and extinction processes. Incorporating complex reaction kinetics could results in predictions of lower flame temperature and therefore more accurately predict lean blow-out.

References

[1] E. E. Zukoski. *Flame stabilization on bluff bodies at low and intermediate Reynolds numbers*. PhD thesis, California Institute of Technology, 1954.

[2] Derek Dunn Rankin, editor. *LEAN COMBUSTION: Fundamentals, Applications, and Prospects*. Academic Press, 2007.

[3] D. C. Wilcox. *Basic Fluid Mechanics*. DWC Industries Inc., 5 edition, Decemeber 2012.

[4] P. Bradshaw. Effects of streamline curvature on turbulent flows. *Advisory Group For Aerospace Research and Development*, AGARDograph No. 169, 1973.

[5] D. C. Wilcox. *Turbulence Modeling for CFD*. DWC Industries Inc., 3 edition, November 2006.

[6] P. Cocks, V. Sankaran, and M. Soteriou. Is les of reacting flows predictive. part 1: Impact of numerics. 51st AIAA Aerospace Sciences Meeting Including The New Horizons Forum and Aerospace Exposition, AIAA Paper 2013-0170, Grapevine, TX, 2013.

[7] T Poinsot and D. Veynante. *Theoretical and numerical combustion*. R.T. Edwards Inc., Philadelphia, PA, 2 edition, 2005.

[8] N. Peters. *Turbulent Combustion*. Cambridge University Press, Cambridge, UK, 2000.

[9] J. Foster. Survey of turbulent combustion models for large eddy simulations of propulsive flowfields. AIAA Science and Technology Forum and Exposition, AIAA Paper 2000-1379, 2000.

[10] A. R. Kerstein. Linear-eddy modelling of turbulent transport. ii application to shear layer mixing. *Combustion and Flame*, 75:397–413, 1989.

[11] A. R. Kerstein. Linear-eddy modelling of turbulent transport. part 6. microstructure of diffusive scalar mixing fields. *Journal of Fluid Mechanics*, 231:361–394, October 1991.

[12] P. McMurthy, S. Menon, and A. Kerstein. A linear eddy sub-grid model for turbulent reacting flows:application to hydrogen-air combustion. volume 24 of *Combustion Institute*, pages 271–278, 1992.

[13] P. McMurthy, S. Menon, and A. Kerstein. Linear eddy modeling of turbulent combustion. volume 7 of *Energy and Fuels*, pages 817–826, 1993.

[14] N. Patel and S. Menon. Simulation of spray-turbulence-flame interactions in a lean direct injection combustor. *Combustion and Flame*, 153:228–257, 2007.

[15] V. K. Chakravarthy and S. Menon. Linear eddy simulations of reynolds number and schmidt number effects on turbulent scalar mixing. *Physics of Fluids*, 13(2):488, 2000.

[16] V. Chakravarthy and S. Menon. Large-eddy simulations of turbulent premized flames in the flamelet regime. *Combustion Science and Technology*, 162:175–222, 2001.

[17] S. B. Pope. Pdf methods for turbulent reactive flows. *Progress in Energy and Combustion Sciences*, 11:119–192, 1985.

[18] S. B. Pope. Self-conditioned fields for large-eddy simulations of turbulent flows. *Journal of Fluid Mechanics*, 652:139–169, 2010.

[19] D. C. Haworth. Progress in probability density function methods for turbulent reacting flows. *Progress in Energy and Combustion Science*, 36:168–259, 2010.

[20] M. R. H. Sheikhi, T. G. Drozda, P. Givi, F. A. Jaberi, and S. B. Pope. Large eddy simulation of a turbulent nonpremixed piloted mathane jet flame. *Proceedings of the Combustion Institute*, 30:549–556, 2005.

[21] D. C. Haworth and S. B. Pope. *Transported Probability Density Function Method for Reynolds-Averaged and Large-Eddy Simulations*, pages 119–142. Springer, 2011.

[22] Viswanathan, S. Wang, and S. B. Pope. Numerical implementation of mixing and molecular transport in les/pdf studies of turbulent reacting flows. *Journal of Computational Physics*, 230:6916–6957, 2011.

[23] R. McDermott and S. B. Pope. A particle formulation for treating differential diffusion in filtered density functions methods. *Journal of Computational Physics*, 226:947–993, September 2007.

[24] S Menon and A. R. Kerstein. *The Linear-Eddy Model*, pages 221–247. Springer, 2011.

[25] R. R. Erickson and M. C. Soteriou. The influence of reactant temperature on dynamics of bluff body stabilized premixed flames. *Combustion and Flame*, 158:2441–57, 2011.

[26] A. M. Briones, B. Sekar, H. J. Thornburg, and K. O. Granlund. V-gutter stabilized turbulent premixed flame and lean blowout. ISABE-2011-1110. International Society for Air-breathing Engines Conference, Goteborg, Sweden, 2011.

[27] A. Sjunnesson, S. Olovsson, and B. Sjoblom. Validation rig - a tool for flame studies. International Society for Air-breathing Engines Conference, Nottingham, United Kingdom, Nottingham, United Kingdom, 1991.

[28] A. Sjunnesson, C. Nelsson, and E. max. LDA measurements of velocities and turbulence in a bluff body stabilized flame. Fourth International Conference on Laser Anemometry - Advances and Application, ASME, Cleveland, OH.

[29] A. Sjunnesson, A. Henrikson, and C. Lofstrom. CARS measurements and visualization of reacting flows in a bluff body stabilized flame. 28th Joint Propulsion Conference and Exhibit, AIAA Paper 1992-3650, Nashville, TN, 1992.

[30] P. Cocks, V. Sankaran, and M. Soteriou. Towards predictive reacting flow les. 52nd Aerospace Sciences Meeting, National Harbor, MD, 2014.

[31] C. Fureby and S. I. Moller. Large-eddy simulation of reacting flows applied to bluff-body stabilized flames. *AIAA Journal*, 33(12):2339–47, 1995.

[32] C. Fureby. A comparison of flamelet LES models for premixed turbulent combustion. 44th AIAA Aerospace Sciences Meeting and Exhibit, AIAA Paper 2006-155, Reno, NV, 2006.

[33] E. Baudoin, R. Yu, Bai, K.J. Nogenmyr, X.S. Bai, and C. Fureby. Comparison of les models applied to a bluff body stabilized flame. 47th AIAA Aerospace Sciences Meeting Including The New Horizons Forum and Aerospace Exposition, AIAA Paper 2009-1178, Orlando, FL, 2009.

[34] I. Porumbel and S. Menon. Large eddy simulation of bluff-body stabilized premixed flames. AIAA Paper 2007-1413. 44th AIAA Aerospace Sciences Meeting, Reno, NV, 2006.

[35] W. P. Jones, A. J. Marquis, and F. Wang. Large eddy simulation of a premixed propane turbulent bluff body flame using the eulerian stochastic field method. *Fuel*, 140:514–25, 2014.

[36] P. Gokulakrishnan, R. Bikkani, M. S. Klassen, R.J. Roby, and B. V. Kiel. Influence of turbulence-chemistry interaction in blow-out predictions of bluff-body stabilized flames. AIAA-2009-1179. 47th AIAA Aerospace Sciences Meeting, Orlando, FL, 2009.

[37] B. Kiel. A detailed investigation of bluff body stabilized flames. 45th AIAA Aerospace Sciences Meeting and Exhibit, Reno, NV, 2007.

[38] G. M. Goldin. Evaluation of les subgrid reaction models in a lifted flame. 43rd AIAA Aerospace Sciences Meeting, AIAA Paper 2005-555, Reno, NV, 2005.

[39] B.F. Magnussen. The eddy dissipation concept: A bridge between science and technology. ECCOMAS Thematic Conference on Computational Combustion, Lisbon, 2005.

[40] F. Ma, W. Proscia, V. Ivanov, and F. Montanari. Large eddy simulation of self-excited combustion dynamics in a bluff-body combustor. 51st AIAA Joint Propulsion Conference. Propulsion and Energy Forum, 2007.

[41] C. Yoon, R. Gejji, , and W. E. Anderson. Computational investigation of combustion dynamics in a lean direct injection gas turbine combustor. 51st AIAA Aerospace Sciences Meeting, AIAA Paper 2013-166, 2013.

[42] M. E. Harvazinski. *Modeling Self-Excited Combustion Instabilities Using a Combination of Two and Three-Dimensional Simulations*. PhD thesis, Purdue University, 2012.

[43] S. Menon and N. Patel. Subgrid modeling for simulation of spray combustion in large-scale combustors. *AIAA Journal*, 44(4), April 2006.

[44] M. Frenklach, H. Wang, C.L. Yu, M. Goldenberg, C.T. Bowman, R.K. Hanson, D.F. Davidson, E.J. Chang, G.P. Smith, D.M. Golden, W.C. Gardiner, V. Lissianski, and http://www.me.berkeley.edu/gri_mech/. Gas Research Institute Topical Report M. Frenklach, H. Wang, M. Goldenberg, G.P. Smith, D.M. Golden, C.T. Bowman, R.K. Hanson, W.C. Gardiner and V. Lissianski. 'GRI-MECH–An Optimized Detailed Chemical Reaction Mechanism for Methane Combustion,' Report No. GRI-95/0058. November 1,1995.

[45] I. Porumbel. *Large Eddy Simulation of bluff body stabilized premixed and partially premixed combustion*. PhD thesis, Georgia Institute of Technology, 2006.

[46] C. Westbrook and F. Dryer. Simplified reaction mechanisms for the oxidation of hydrocarbon fuels in flames. *Combustion Science and Technology*, 27:31–43, 1981.